Prostaglandin E_2 controls the metabolic adaptation of T cells to the intestinal microenvironment

Matteo Villa[1,2], David E. Sanin[1,3], Petya Apostolova[1,3,4], Mauro Corrado[1,5,6,7], Agnieszka M. Kabat[1,3], Carmine Cristinzio[1,8], Annamaria Regina[1,9], Gustavo E. Carrizo[1], Nisha Rana[1], Michal A. Stanczak[1], Francesc Baixauli[1], Katarzyna M. Grzes[1], Jovana Cupovic[1], Francesca Solagna[1], Alexandra Hackl[1], Anna-Maria Globig[10], Fabian Hässler[1], Daniel J. Puleston[1], Beth Kelly[1], Nina Cabezas-Wallscheid[1], Peter Hasselblatt[10], Bertram Bengsch[10,11], Robert Zeiser[4,11], Sagar[10], Joerg M. Buescher[1], Edward J. Pearce[1,3,11,12,13] and Erika L. Pearce[1,3,11,14].

Affiliations

1. Max Planck Institute for Immunobiology and Epigenetics, 79108 Freiburg - Germany
2. Division of Rheumatology and Immunology, Department of Internal Medicine, Medical University of Graz, 8036 Graz - Austria
3. Bloomberg-Kimmel Institute of Immunotherapy, Department of Oncology, Johns Hopkins University School of Medicine, Baltimore - USA
4. Department of Medicine I (Hematology and Oncology), University Medical Center Freiburg, 79106 Freiburg - Germany
5. Cologne Excellence Cluster on Cellular Stress Responses in Aging-Associated Diseases (CECAD), University of Cologne, Cologne - Germany
6. Center for Molecular Medicine (CMMC), University of Cologne, Cologne - Germany
7. Institute for Genetics, University of Cologne, Cologne - Germany
8. Department of Medical Biotechnology, University of Siena, Siena - Italy
9. Department of Life Sciences, University of Trieste, 34128 Trieste - Italy
10. Department of Medicine II, University Medical Center Freiburg, 79106 Freiburg - Germany
11. CIBSS Centre for Integrative Biological Signalling Studies, Freiburg - Germany
12. Faculty of Biology, University of Freiburg, 79104 Freiburg - Germany
13. Department of Molecular Microbiology and Immunology, Bloomberg School of Public Health, Johns Hopkins University, Baltimore - USA
14. Department of Biochemistry and Molecular Biology, Bloomberg School of Public Health, Johns Hopkins University, Baltimore - USA

Corresponding Author: Erika L. Pearce, E-mail: epearce6@jhmi.edu; Matteo Villa, E-mail: matteo.villa@medunigraz.at.

Abstract

Immune cells must adapt to different environments during the course of an immune response. We studied the adaptation of CD8$^+$ T cells to the intestinal microenvironment and how this process shapes their residency in the gut. CD8$^+$ T cells progressively remodel their transcriptome and surface phenotype as they acquire gut residency, and downregulate expression of mitochondrial genes. Human and mouse gut-resident CD8$^+$ T cells have reduced mitochondrial mass, but maintain a viable energy balance to sustain their function. We found that the intestinal microenvironment is rich in prostaglandin E_2 (PGE_2), which drives mitochondrial depolarization in CD8$^+$ T cells. Consequently, these cells engage autophagy to clear depolarized mitochondria, and enhance glutathione synthesis to scavenge reactive oxygen species (ROS) that result from mitochondrial depolarization. Impairing PGE_2 sensing promotes CD8$^+$ T cell accumulation in the gut, while tampering with autophagy and glutathione negatively impacts the T cell population. Thus, a PGE_2-autophagy-glutathione axis defines the metabolic adaptation of CD8$^+$ T cells to the intestinal microenvironment, to ultimately influence the T cell pool.

Main

The immune response is dynamic. Immune cells are activated, migrate, and perform effector functions in tissues characterized by different chemical and physical properties. In peripheral organs, immune cells surveil for pathogens as well as contribute to tissue homeostasis. At barrier sites such as the gut, immune cells are key to maintaining the symbiosis between host and microbiota, the breach of which promotes the development of inflammatory bowel disease (IBD). Understanding the mechanisms that control the adaptation of immune cells to the tissue niche is an important step toward identifying strategies to modulate immune function and designing mucosal vaccines against infections and cancer [1].

To investigate how immune cells adapt to their microenvironment, we explored the intestinal CD8$^+$ T cell response [2, 3]. Upon activation in response to foreign antigens from the gut, naive CD8$^+$ T cells (T_N) in the mesenteric lymph nodes (mLN) differentiate into effector/effector memory T cells (T_{EM}) or central memory T cells (T_{CM}). Differentiation into memory T cells is accompanied by transcriptional and metabolic reprogramming, which in turn underlie the characteristic features of these cells [4-7]. T_{EM} leave the lymph nodes and enter the blood stream to reach target organs (reviewed in [8]). There, after clearing the antigen that initiated the immune response, only a small proportion of T_{EM} survive; some continue to circulate in and out of peripheral tissues, while others acquire residency in the intestine. Moreover, during the early phases of the immune response, a fraction of CD8$^+$ T cells commits to the tissue-resident memory T cell (T_{RM}) fate, eventually seeding the gut tissue [9, 10]. These long-lived and sessile cells constitute the front-line defense against future encounters to the same antigen [11-14]. The cytokines interleukin-15 (IL-15) and tissue growth factor-β (TGF-β), together with a network of transcription factors, coordinate the development of T_{RM} [15-19].

While a conserved transcriptional network may underlie the generation of T_{RM} across tissues, it is reasonable to hypothesize that adaptation of T cells to the gut environment influences the establishment of the intestinal CD8$^+$ T cell pool, including T_{RM}. Indeed, some of the metabolic requirements of T_{RM} are not shared across all tissues of residence, highlighting that tissue-specificity could impact metabolism [20, 21]. Further, the surrounding microenvironment has been shown to influence the fate and function of CD8$^+$ T cells. For instance, nutrient availability as well as cell-intrinsic metabolic programs impinge on fitness and function of tumor-infiltrating CD8$^+$ T cells [22-25]. Similarly, tissue-specific cues regulate the transcriptional landscape and surface phenotype of T cells, thus influencing their residency [26, 27]. These examples highlight how a variety of factors control the ability of T cells to adapt to and thrive in the surrounding environment.

Using single cell RNA sequencing and oligo-tagged antibody staining, we resolved the transcriptional

and metabolic adaptation of CD8$^+$ T cells to the intestinal microenvironment. Upon sensing prostaglandin E_2 (PGE_2) in the gut tissue, CD8$^+$ T cells decreased their mitochondrial content. PGE_2 induced mitochondrial depolarization in CD8$^+$ T cells, and as a consequence, CD8$^+$ T cells enhanced their antioxidant capability and engaged autophagy to clear mitochondria. Our findings further the knowledge of how the intestinal CD8$^+$ T cell pool is established, define a precise metabolic adaption of T cells in a tissue, and highlight novel therapeutic avenues to modulate immune function in a tissue-restricted fashion.

Results

Transcriptional and surface profile differences underlie the adaptation of CD8$^+$ T cells to the intestinal microenvironment

To study the tissue adaptation of CD8$^+$ T cells, we focused on cells in the small intestine under homeostatic conditions. By combining cell sorting, single cell RNA sequencing, and oligo-tagged antibody sequencing, we analyzed the transcriptome and surface proteome of CD8$^+$ T cells from the mesenteric lymph node (mLN), lamina propria (LP) and intraepithelial lymphocyte fraction (IEL, concentrating on CD8$\alpha\beta$ induced IEL) of the gut (**Fig. 1a** and **Extended Data Fig. 1a**), presuming that we would capture the transition of these cells across these sites under homeostatic conditions. To assess the tissue-resident nature of LP-isolated cells we used *in vivo* intravascular staining and found that CD8$^+$ T cells isolated from the gut LP were virtually free of cells associated with blood vessels [28] (**Extended Data Fig. 1b**). Integrating the RNA and surface protein landscapes of 49,111 cells across 3 biological replicates we identified 10 clusters visualized on the uniform manifold approximation and projection (UMAP)-reduced dimensional space (**Fig. 1b**). Cell clusters were present in all biological replicates (**Extended Data Fig. 1c**) and displayed unique transcriptional and protein expression profiles (**Fig. 1c, d**). In accordance with our sorting strategy, cluster 6 expressed *Sell*, *Klf2,* and *S1pr1* (**Fig. 1c**), which control retention of CD8$^+$ T cells in lymphoid organs [29], and CD62L, pointing to their residence in mLN (**Fig. 1d**). Expression of *Rora*, previously associated with intestinal residency [30], was observed in clusters 1 and 2, which also displayed increased expression of the immunomodulatory, adenosine-producing enzymes CD38 and CD39 (**Fig. 1d**) [31]. Granzyme-encoding genes *Gzma* and *Gzmb* expression was increased in cluster 0 (**Fig. 1c**), as well as CD103 and Integrin-β7, that help the positioning of T_{RM} in the gut (**Fig. 1d**). Cells associated to clusters 0 and 5 also expressed CD326, better known as EpCAM, recently shown to be associated with IEL origin, to support the movement of T cells within the epithelial layer (**Fig. 1d**, [32]). Finally, expression of *Lgals1* hinted at the ability of cells within cluster 7 to interact with the extracellular matrix (**Fig. 1c**). These results highlighted the diversity of CD8$^+$ T populations in the sites studied. Exploration of the tissue origin of the samples placed T_N and T_{CM} in close proximity to mLN T_{EM} on the UMAP, whereas LP-resident CD8$^+$ T cells were between mLN T_{EM} and IEL-resident CD8$^+$ T cells (**Fig. 1e**). Few clusters were shared between tissues, with cluster 6 almost exclusively populated by T_N and T_{CM} mLN cells; clusters 1, 2, and 4 were characteristic of LP, and clusters 0 and 5 originated mostly from the IEL fraction (**Fig. 1f**). A notable exception was cluster 7, which was distributed across both mLN and LP, suggesting a potential seeding point of mLN-activated CD8$^+$ T cells in the intestinal wall (**Fig. 1f**). Altogether, we identified a substantial heterogeneity in the transcriptional landscape and surface profile of CD8$^+$ T cells across the mLN-LP-IEL axis.

CD8$^+$ T cells entering the intestine exhibit an altered transcriptome with reduced expression of mitochondria-related genes

The single cell analysis highlighted that CD8$^+$ T cell adaptation to the intestinal microenvironment correlated with remarkable changes in the expression of mitochondria-encoded genes (**Fig. 2a**). To better explore how these changes were regulated across the clusters identified in Figure 1b, we ranked CD8$^+$ T cells during their transition from the mLN to the gut according to transcriptional similarity using Slingshot [33]. We calculated the average pseudotime estimation for each cell based on all predicted trajectories, setting cells in cluster 6 as the origin of the progression based on our cell sorting strategy. In this manner, we ordered cells based on estimated pseudotime (**Extended Data Fig. 2a**). Accordingly, clusters in the LP and IEL appeared later in this progression and were characterized by a higher pseudotime value (**Extended Data Fig. 2a**). When we plotted the expression profiles of several mitochondria-encoded transcripts as a function of pseudotime, we found that CD8$^+$ T cells progressively decreased their expression during the transition from mLN to LP and ultimately to IEL (**Fig. 2b**, **c**). Of note, the progressive reduction of gene expression across pseudotime was not a generalized phenomenon, since a number of genes relevant to CD8$^+$ T cell physiology followed different expression patterns during the transition from mLN to intestine (**Extended Data Fig. 2b**). In conclusion, CD8$^+$ T cells transiting from the mLN to the intestinal wall exhibited reduced expression of mitochondria-encoded transcripts.

Residency in the intestine reduces the mitochondrial content in CD8$^+$ T cells

To further explore the results we acquired from our single cell sequencing analyses, we obtained blood and intestinal biopsies from healthy human donors and isolated CD8$^+$ T cells (**Extended Data Fig. 3a**). We used flow cytometry to assess mitochondrial content in T_N, T_{EM}, CD45RA-expressing T_{EM} (T_{EMRA}), and T_{CM} isolated from the blood and T_{RM} from the gut, by labeling with the mitochondria-selective dye Mitotracker green. T_{RM} isolated from different areas of the gut showed a substantially reduced Mitotracker green staining as compared to blood-resident CD8$^+$ T cell populations, recapitulating of our findings in humans (**Fig. 3a**).

To further investigate the relationship between the adaptation of CD8$^+$ T cells to the intestinal tissue and the reduction of mitochondrial mass, we explored the physiological CD8$^+$ T cell gut immune response in naive mice (**Extended Data Fig. 3b**, further details about the gating strategy and the nomenclature used throughout the manuscript are in the “FACS” paragraph of the Methods section). Supporting the single cell data showing reduced mitochondrial transcripts, and the human data (**Fig. 3a**), we found that CD8$^+$ T cells exhibited progressively reduced Mitotracker green staining during the transition from mLN-resident subsets (T_N, T_{EM}, T_{CM} and T_{RM}) to the LP and IEL, highlighting an inflection point between the CD69$^-$CD103$^-$ to CD69$^+$CD103$^+$ transition in the LP (**Fig. 3b**). Honing in on the LP, and on the transition from CD69$^-$CD103$^-$ cells, to CD69$^+$CD103$^-$ cells, and finally to CD69$^+$CD103$^+$ cells [17], it became apparent that reduced Mitotracker green staining only occurred upon acquisition of the *bona fide* T$_{RM}$ profile in the gut (CD69$^+$CD103$^+$) (**Extended Data Fig. 3c**). Of note, the reduction in mitochondrial content upon acquisition of residency in the gut, as measured by Mitotracker green staining, was independent of the differential activity of mitochondrial efflux pumps (treatment with verapamil, a blocker of the xenobiotic efflux pumps encoded by *Bcrp1* and *Mdr1a/b*) [34] or cell death (treatment with KN-62, which prevents cell death triggered by ATP and/or NAD-induced activation of the P2RX7 receptor during tissue preparation) between mLN and gut-isolated CD8$^+$ T cells [35] (**Extended Data Fig. 3d, e**). Confirming the Mitotracker green data, western blot analysis showed reduced expression of the mitochondrial structural protein TOM20 and the mitochondria-specific transcription factor TFAM in CD8$^+$ T cells isolated from the LP and IEL as compared to cells from the mLN (**Fig. 3c** and **Extended Data Fig. 3f**). Taken together our data show that gut resident T cells have reduced mitochondrial content.

To confirm our results in an antigen-specific setting, we transferred CD90.1$^+$ ovalbumin (OVA)-specific CD8$^+$ T cells into CD90.1$^-$ recipient mice, and infected them orally with a transgenic strain of *Listeria monocytogenes* expressing OVA (*LmOVA*), to study the OVA-specific intestinal CD8$^+$ T cell response. OVA-specific CD8$^+$ T cells isolated 7 and 24 days post-infection from the LP and IEL of infected mice showed substantially reduced mitochondrial content as compared to OVA-specific cells isolated from the mLN, mirroring the results obtained from the analysis of the polyclonal response (**Fig. 3d** and **Extended Data Fig 4a**).

Since mitochondrial dynamics (fission *vs* fusion) has been linked to T cell fate acquisition [4], we isolated CD8$^+$ T cells from the mLN, LP, and IEL of PhAM mice, expressing the mitochondria-localized version of the fluorescent protein Dendra2 [36], and assessed their mitochondrial morphology using live cell imaging. In keeping with our other findings assessing mitochondrial content, imaging software found that CD69$^+$CD103$^+$ cells isolated from the LP and IEL showed reduced numbers of mitochondria as compared to spleen- and mLN-isolated T cell populations (**Extended Data Fig. 4b**). Moreover, mitochondria of gut-resident CD8$^+$ T cells were fragmented and shared similarities with mLN-isolated T$_{EM}$, as compared to T$_N$ or T$_{CM}$, previously shown to form complex networks of fused mitochondria [4] (**Extended Data Fig. 4b**). Western blot analysis of the distribution of OPA-1 isoforms, with the relative accumulation of the shortest being associated with mitochondrial fragmentation [37], correlated with the data obtained from PhAM mice (**Extended Data Fig. 4c**). Finally, transmission electron microscopy analysis to assess mitochondrial ultrastructure showed that mitochondria present in gut-isolated cells had dilated cristae, as compared to mLN-resident cells (red arrowheads, **Extended Data Fig. 4d**), supporting the data regarding the distribution of the OPA-1 isoforms. Altogether, these data corroborate the finding that gut-resident cells have a fragmented mitochondrial network, as compared to CD8$^+$ T cells localized in the mLN.

We next tested whether reduced mitochondrial mass was accompanied by defective mitochondrial function. We used TMRM to assess mitochondrial membrane potential across the inner mitochondrial membrane, as a readout of the functionality of the electron transport chain (ETC) and movement of protons across the inner mitochondrial membrane. Analysis of CD8$^+$ T cells across the physiological intestinal immune response showed that gut-resident cells had reduced mitochondrial membrane potential when compared to cell populations resident in the mLN, mirroring the staining pattern observed for Mitotracker green (**Fig. 3e**). Similarly, we found that the mitochondrial membrane potential of gut-isolated antigen-specific CD8$^+$ T cell subsets was reduced in comparison to the one recorded in mLN-isolated cells (**Fig. 3f**). Notwithstanding the reduction of mitochondrial mass, gut-resident cells were able to effectively engage the ETC in the remaining mitochondria to produce ATP, as shown by TMRM staining increasing after inhibition of the ATP synthase by oligomycin, an effect dissipated by the uncoupling agent FCCP (**Fig. 3g**). CD69$^+$CD103$^+$ T cells isolated from the gut, LP in particular, had a significantly lower ATP/AMP ratio, but did not have significant defects in their energy balance, as measured by AMP, ADP, and ATP levels, as compared to cells isolated from mLN (**Fig. 3h**). To assess the potential impact of mitochondrial loss over the function of CD8$^+$ T cells, we analyzed a mouse model that uses eYFP to report one-to-one interferon-γ protein expression, without requiring restimulation of cells (GREAT mice [38]). We found that the reduction of mitochondrial mass observed in gut-resident CD8$^+$ T cells did not necessarily lead to defective cytokine production, as most of the cells isolated from the LP and IEL produced interferon-γ (**Fig. 3i**).

To complement our analysis, we performed in depth transcriptional profiling using bulk RNA sequencing of the different CD8$^+$ T cell populations. Principal component analysis (PCA) of their transcriptome positioned the cell populations in a progression from more quiescent populations (mLN-isolated T_N, T_{CM} and T_{RM}) to activated ones (mLN-isolated T_{EM}) and ultimately to populations isolated from the intestinal wall (LP and IEL-isolated CD69$^-$CD103$^-$ cells and CD69$^+$CD103$^+$ cells) (**Extended Data Fig. 4e**). As with our single cell analyses, we observed that T_N and T_{CM} clustered together, and were separated from the tissue populations by T_{EM}. Moreover, LP populations laid between mLN and IEL cells, thus validating our earlier observations and trajectories (**Extended Data Fig. 4e**). When we analyzed the differentially expressed genes (DEGs) across the cell subsets, we found that adaptation of CD8$^+$ T cells to the LP triggered a transient global upregulation of transcripts (transition 3), whereas acquisition of the CD69$^+$CD103$^+$ T_{RM} phenotype (transitions 4 and 5) caused downregulation of the transcriptome (**Extended Data Fig. 4f**). Moreover, bulk RNA sequencing confirmed the transcriptional signature identified in Figure 2, as transcripts involved in mitochondrial function showed broad downregulation during the transition between mLN T_{EM} and LP CD69$^+$CD103$^+$ cells (**Extended Data Fig. 4g**). Overall, we found that adaptation of CD8$^+$ T cells to the intestinal microenvironment correlates with reduced mitochondrial mass, membrane potential, and fragmentation of the mitochondrial pool. In spite of this, gut-resident CD8$^+$ T cells maintained functionality of the remaining mitochondria to sustain a viable energy balance and cytokine production.

Prostaglandin E_2 regulates mitochondrial content and fitness of gut-resident T cells

Resident CD8$^+$ T cells are distributed across nearly all peripheral organs. To test if the reduction of mitochondrial content is a phenomenon restricted to the gut or occurs in other tissues, we measured Mitotracker green uptake in CD8$^+$ T cells isolated from the parenchyma of liver and lung. We found that gut-resident CD69$^+$CD103$^+$ cells displayed substantially reduced mitochondrial mass as compared to counterparts isolated from mLN as well as from liver and lung (**Fig. 4a**). Interestingly, gut-resident macrophages did not show any reduction of mitochondrial content as compared to other tissues, showing that the phenotype was not common to all immune cells in the intestine (**Extended Data Fig. 5a**).

To investigate how the intestinal microenvironment might regulate the mitochondrial content of CD8$^+$ T cells, we isolated the interstitial fluid of several tissues and analyzed the fluid using untargeted metabolomics. The analysis revealed a group of metabolites uniquely present in the small intestine, including prostaglandin E_2 (PGE_2) (**Fig. 4b, c**). PGE_2 signaling is constitutive in the gut and it contributes to tissue repair and maintenance of the epithelial barrier [39, 40]. Also, we recently reported that PGE_2 controls mitochondrial membrane potential in macrophages [41]. To test the role of PGE_2 in driving the reduction of mitochondrial content in CD8$^+$ T cells, we established an *in vitro* model to partly mimic the commitment of CD8$^+$ T cells towards tissue residence, and we referred to these cells as (IL-15/TGF-β)-T cells (**Extended Data Fig. 5b**). Treatment with IL-15 and TGF-β induced a phenotype characterized by high expression of the integrin CD103, as compared to cells treated with IL-2 [(IL-2)-T cells] (**Extended Data Fig. 5c**). (IL-15/TGF-β)-T cells substantially reduced their mitochondrial mass and membrane potential upon PGE_2 exposure, similar to what we observed for CD8$^+$ T cells acquiring residence in the intestine (**Fig. 4d**). Also, (IL-15/TGF-β)-T cells seemed to be more sensitive to the effect of PGE_2 treatment on mitochondrial content, as compared to (IL-2)-T cells (**Extended Data Fig. 5d, e**). The effect of PGE_2 was dependent on its concentration, with as little as 10 nM PGE_2 triggering the reduction of mitochondrial mass and membrane potential in (IL-15/TGF-β)-T cells (**Extended Data Fig. 5f**). Finally, the reduction of mitochondrial content in (IL-15/TGF-β)-T cells was specifically triggered by PGE_2 and PGE_1, while exposure to other prostaglandins did not cause any noticeable effect (**Fig. 4e**). Since PGE_2 and PGE_1 both signal through EP1-4 receptors, we analyzed receptor expression *in vivo* across CD8$^+$ T cell subsets. We found that *Ptger4*, encoding for the EP4 receptor, was uniquely upregulated in CD8$^+$ T cells isolated from the gut (**Extended Data Fig. 5g**). Moreover, the single cell data confirmed that *Ptger4* transcripts were substantially upregulated in cells occupying the UMAP space of LP and IEL, as compared to cells positioned in the "mLN area" (**Fig. 4f**). CRISPR-Cas9 mediated *Ptger4* deletion impinged on the ability of (IL-15/TGF-β)-T cells to sense PGE_2 and partially rescued the reduction of mitochondrial content and function (**Extended Data Fig. 5h**, **i**).

To investigate whether PGE_2-driven reduction of mitochondrial content controls the adaptation of $CD8^+$ T cells to the gut and the establishment of the T cell pool, we tested the effect of *Ptger4* deletion in the generation of gut-resident $CD8^+$ T cells following oral *Listeria monocytogenes* infection. Recipient mice were co-transferred with control (Ctrl) or *Ptger4*-deficient naive ovalbumin (OVA)-specific $CD8^+$ T cells that expanded in response to oral challenge with a transgenic strain of *Listeria monocytogenes* expressing ovalbumin (*LmOVA*) (**Fig. 4g**). *Ptger4*-deficient cells outcompeted control cells in establishing the antigen-specific pool of $CD8^+$ T cells in the LP and in the induced-IEL fraction, upon oral infection with *LmOVA*, whereas no such difference was observed in mLN (**Fig. 4h, i, Extended Data Fig. 5j**). Moreover, *Ptger4*-deficient $CD69^+CD103^+$ cells isolated from LP showed higher mitochondrial content, as compared to control counterparts (**Fig. 4j**). Interestingly, *Ptger4*-deficient cells were more prone to retain the $CD69^-CD103^-$ phenotype, as compared to control cells, and fewer of them progressed to the $CD69^+$ stage (**Fig. 4k**). On the other hand, deletion of *Ptger4* only minimally affected the ability of gut-isolated $CD8^+$ T cells to produce interferon-γ and TNF (**Extended Data Fig. 5k**). These data show that the loss of mitochondrial content is, at least in part, consequence of being in an environment rich in PGE_2, and disruption of PGE_2 sensing promotes accumulation of $CD8^+$ T cells in the intestinal wall. Altogether, we found that the intestinal microenvironment triggered reduction of the mitochondrial content of $CD8^+$ T cells. We also identified PGE_2 as one of the causative agents initiating this process.

Autophagy and glutathione counterbalance the effect of PGE_2 and maintain the pool of gut-resident T cells

Next, we addressed the issue of how PGE_2 exposure influenced the mitochondrial content of $CD8^+$ T cells. Mitochondria are important regulators of cell function. These organelles routinely undergo quality control to test their fitness, and dysfunctional mitochondria are cleared by mitophagy, *i.e.* mitochondrial autophagy (reviewed in [42]). A drop in mitochondrial membrane potential has been shown to trigger clearance of depolarized mitochondria [43]. Since we showed that PGE_2 contributed to the reduction of mitochondrial membrane potential, we hypothesized that mitochondrial depolarization may trigger autophagy-mediated clearance of mitochondria in gut-resident $CD8^+$ T cells. Indeed, $CD8^+$ T cells upregulated most of the autophagy-related genes (*Atg* genes) as well as *Optn*, *Prkn*, *Sqstm1*, *Ulk1* and *Pink1*, associated with mitophagy, during their transition from mLN to the intestinal wall (**Fig. 5a**). $CD69^+CD103^+$ cells isolated from LP and IEL expressed the lipidated form of LC3 (LC3-II), uniquely formed upon autophagy initiation (**Fig. 5b**). Treating intestinal $CD8^+$ T cells with the autophagy inhibitor bafilomycin A1 inhibited autophagic flux and drove accumulation of the lipidated form of LC3, suggesting that LP- and IEL-isolated CD69$^+$CD103$^+$ cells actively engaged autophagy (**Extended Data Fig. 6a**). Moreover, CD8$^+$ T cells isolated from the intestine showed reduced expression of p62, encoded by *Sqstm1*, which is degraded in the autophagy process (**Fig. 5b** and **Extended Data Fig. 6b**). Finally, transmission electron microscopy provided further evidence that gut-isolated CD8$^+$ T cells upregulated autophagy, as structures resembling autophagosomes were identified only in images of LP CD69$^+$CD103$^+$ and IEL T$_{RM}$ (**Fig. 5c**). Treating (IL-15/TGF-β)-T cells with bafilomycin A1 partially blunted the reduction of mitochondrial mass observed upon PGE$_2$ treatment, but failed to rescue the reduction of mitochondrial membrane potential, suggesting that inhibition of autophagy prevented mitochondrial clearance while leaving PGE$_2$ sensing and the subsequent drop of mitochondrial membrane potential unaffected (**Fig. 5d**). Inhibition of autophagy with wortmannin, a PI3K inhibitor, or SBI-0206965, an ULK1 inhibitor, equally prevented mitochondrial clearance upon treatment with PGE$_2$ (**Extended Data Fig. 6c, d)**. However, both wortmannin and SBI-0206965 also rescued the PGE$_2$-driven reduction of mitochondrial membrane potential (**Extended Data Fig. 6c, d**). Finally, we tested whether autophagy plays a role in the formation of the pool of gut-resident CD8$^+$ T cells upon oral challenge with *LmOVA*. We blocked autophagy by deleting *Atg5* with CRISPR-Cas9 (**Extended Data Fig. 6e**) and found that *Atg5*-deficient CD8$^+$ T cells failed to establish the antigen-specific pool of CD8$^+$ T cells in LP and induced IEL fraction, as compared to control cells (**Fig. 5e, f**). No consistent changes in the distribution of Ctrl vs *Atg5*-deficient cells were observed in the pool of antigen-specific CD8$^+$ T cells in mLN (**Extended Data Fig. 6f**). In line with our *in vitro* results using bafilomycin (**Fig. 5d**), genetically blocking autophagy partially prevented mitochondrial clearance in *Atg5*-deficient LP CD69$^+$CD103$^+$ cells, as compared to controls (**Fig. 5g**). These results suggest that failure to clear depolarized mitochondria in gut-resident, PGE$_2$-exposed CD8$^+$ T cells negatively impacts the fitness of the intestinal CD8$^+$ T cell pool.

We wondered whether the PGE$_2$-driven reduction in mitochondrial membrane potential resulted in the production of reactive oxygen species (ROS), and thus altered redox balance, in gut-resident CD8$^+$ T cells. We analyzed Mito-roGFP2-Orp1 mice, encoding a mitochondria-targeting redox-sensitive GFP that senses hydrogen peroxide (H_2O_2) [44, 45] and found that CD8$^+$ T cells isolated from the intestinal wall exhibited an increased proportion of cells with oxidized mitochondria, as compared to T$_N$ and T$_{CM}$ cells isolated from mLN, while T$_{EM}$ had the most oxidized mitochondria. (**Fig. 5h** and **Extended Data Fig. 6g**). Although the gut-resident T cells had increased mitochondrial ROS, as quantified in Mito-RoGFP2-Orp1 mice, these cells had low cellular ROS, as quantified by CellROX, compared to the CD8$^+$ T cells resident in the mLN (**Fig. 5i**). Reconciling these seemingly contradicting data, we found that CD8$^+$ T cells isolated from the gut upregulated a panel of genes associated with ‘antioxidant activity’, including genes encoding for glutathione peroxidases (*Gpx* genes), transferases (*Gstm* genes) and reductase (*Gsr*) (**Fig. 5j**). Both the reduced (GSH) and oxidized (GSSG) forms of glutathione were elevated in CD69$^+$CD103$^+$ T cells isolated from LP and

IEL compared to T cells isolated from the mLN, while the GSH/GSSG ratio was unaltered (**Fig. 5k** and **Extended Data Fig. 6h**). These results suggested that upon sensing the gut microenvironment, CD8$^+$ T cells enhance their antioxidant defenses to cope with elevated mitochondrial ROS and maintain a viable intracellular redox balance. To assess the contribution of glutathione in the formation of the intestinal CD8$^+$ T cell pool, we genetically ablated the catalytic subunit of glutamate cysteine ligase (*Gclc*), an enzyme critical for the *de novo* synthesis of glutathione, which has previously been shown to be key to T cell development and function [46, 47] (**Extended Data Fig. 6i**). Similar to what we observed upon autophagy inhibition, *Gclc* deletion remarkably affected accumulation of CD8$^+$ T cells in LP and induced-IEL fractions in mice orally challenged with *LmOVA* (**Fig. 5l, m**). Glutathione thus appears to be key to sustain the redox balance and viability of the intestinal CD8$^+$ T cell pool and to counterbalance the accumulation of ROS resulting from PGE$_2$-driven mitochondrial depolarization.

Got1 links PGE$_2$ with the regulation of mitochondrial content in intestinal CD8$^+$ T cells

To investigate the mechanisms underlying the regulation of mitochondrial content mediated by PGE$_2$, we first assessed whether PGE$_2$ itself was sufficient to promote autophagy. Treatment of (IL-15/TGF-β)-T cells with 100 nM PGE$_2$ induced accumulation of LC3-II, as compared to untreated cells (**Fig. 6a**), suggesting that PGE$_2$ induces autophagy in CD8$^+$ T cells.

As CD8$^+$ T cells resident in the intestine had a fragmented mitochondrial network (**Extended Data Fig. 4**), and mitochondrial fission plays a role in mitophagy, we tested whether *Drp1* was required to mediate the PGE$_2$-driven reduction of mitochondrial content [48]. Mice carrying a *Drp1* deletion in the T cell compartment (*Drp1*$^{f/f}$*CD4*$^{Cre+}$) showed a normal distribution of CD8$^+$ T cells across mLN, LP and IEL compared to littermate controls (*Drp1*$^{f/f}$*CD4*$^{Cre-}$) (**Fig. 6b**). Furthermore, deficiency of *Drp1* did not affect the ability of gut-isolated CD8$^+$ T cells to reduce their mitochondrial content and function upon sensing PGE$_2$ in the gut microenvironment (**Fig. 6c** and **6d**). These data are in line with previous reports suggesting that *Drp1*-mediated mitochondrial fission could be dispensable for mitophagy [49-51].

We used hints from our previous work [41] as a framework to further explore PGE$_2$ regulation of mitochondrial content in intestinal CD8$^+$ T cells. Bulk RNA sequencing showed a strong upregulation of *Got1* in CD69$^+$CD103$^+$ cells isolated from the LP (**Fig. 6e**). This result was confirmed at the single cell level (**Fig. 6f**) and, interestingly, both the datasets highlighted that *Got1* upregulation occurred only in the LP, sparing IEL (**Fig. 6e** and **6f**). *Got1* encodes an enzyme playing a key role in the activity of the malate-aspartate shuttle (MAS), a system that controls redox balance between mitochondria and cytosol. While other enzymes involved in the MAS were not substantially affected in this setting, the MAS metabolite NAD$^+$ was decreased in CD8$^+$ T cells resident in the gut compared to mLN-isolated counterparts (**Fig. 6g**). Reduced NAD$^+$ levels would likely affect function of the NAD$^+$-dependent glycolysis enzyme GAPDH, an important regulator of glycolytic flux. Intestinal CD8$^+$ T cells accumulated metabolites upstream of GAPDH, such as hexose phosphate, fructose 1,6-bisphosphate and dihydroxyacetone phosphate (DHAP), while the levels of phosphoenolpyruvate (PEP), downstream of GAPDH, remained unaffected (**Extended Data Fig. 7a**). All in all, these data build upon our previous work [41] and implicate that intestinal PGE$_2$ may affect the function of MAS, and ultimately shape mitochondrial content and function in CD8$^+$ T cells. To test this hypothesis, we deleted *Got1* in OVA-specific cells (**Extended Data Fig. 7b**), transferred them in recipient mice and assessed if *Got1* played a role in controlling mitochondrial content and function in intestinal CD8$^+$ T cells upon challenge with *LmOVA*. While *Got1* deficiency did not consistently affect the distribution of CD8$^+$ T cells in the LP and IEL (**Extended Data Fig. 7c**), it did affect the ability of CD8$^+$ T cells to reduce their mitochondrial content and function in response to gut entry (**Fig. 6h** and **6i**). Interestingly, the impairment of the reduction of mitochondrial content was observed only in CD69$^-$CD103$^-$ and CD69$^+$ T cells, suggesting that additional mechanisms other than the one mediated by *Got1* could regulate mitochondrial content in CD8$^+$ T cells. Of note, *Got1*-deficient cells were less prone to transit to the CD69$^+$ state, and accumulated as CD69$^-$CD103$^-$ cells (**Fig. 6j**), reminiscent of the effect driven by *Ptger4* deletion (**Fig. 4k**).

In summary, we identified a previously unrecognized mechanism that underlies the adaptation of CD8$^+$ T cells to the intestinal microenvironment. T cells entering the gut sense PGE$_2$, uniquely expressed in the gut during homeostasis, which drives reduction of mitochondrial mass and membrane potential in these CD8$^+$ T cells that express EP4. We propose that PGE$_2$ affects the mitochondrial membrane potential via alterations of the malate-aspartate shuttle, autophagy contributes to the clearance of depolarized mitochondria, whereas glutathione maintains the redox balance in PGE$_2$-responding cells to ultimately shape the pool of gut CD8$^+$ T cells (**Fig. 6k**).

Discussion

Immune responses are initiated in lymphoid tissues, but immune cells carry out their effector function in peripheral tissues. Thus, understanding the adaptation of immune cells to their surrounding environment is key to design new approaches to regulate immunity in a tissue-specific fashion. Investigation of tissue immunity has been hindered by technical limitations that constrain the yield of cells that can be isolated from these tissues and analyzed [52]. Single cell technologies are now providing a way to partially overcome these limitations, and to capture transcriptional changes that may underscore the adaptation of cells to the tissue microenvironment. In this study we used single cell RNA sequencing and oligo-tagged antibody staining to characterize how the intestine-specific $CD8^+$ T cell response unfolds across lymphoid (mLN) and peripheral (LP and IEL) tissues. Of note, our analysis focuses on thymus-selected $CD8\alpha\beta$ T cells, from their naïve stage in mLN, to their terminally-differentiated stage as induced IEL. We took advantage of the constitutive physiological activation of the gut immune response driven by microbiota and food antigens (reviewed in [53]) to investigate the adaptation of T cells to the gut microenvironment. By using this strategy, we overcame the potential alterations of tissue architecture caused by an overt infection that could potentially affect the homeostatic environment of the gut. However, to confirm our findings in an antigen-specific model, we orally challenged mice with *L. monocytogenes*, to assess the adaptation of antigen-specific $CD8^+$ T cells to the gut, and to test how genetic manipulations of the PGE_2-autophagy-glutathione axis affected accumulation of $CD8^+$ T cells in the intestine.

Single cell analysis of the gut $CD8^+$ T cell immune response identified a continuum of transcriptional and surface features that positioned the lamina propria (LP) of the small intestine as a transit site for recently-activated $CD8^+$ T cells (T_{EM}) trafficking from the mLN to the periphery. Despite the limitations inherent to this analysis, such as the "snapshot" nature of it, this finding is in line with the notion that blood vessels that supply the small intestine are embedded within the LP [54], suggesting that this tissue acts as a seeding ground for the whole gut, and is the location where T cell adaption to the gut environment occurs. Our analysis found that gut adaptation is underscored by transcriptional and metabolic changes, prompting the questions of whether and how the gut microenvironment affects the epigenetic landscape of $CD8^+$ T cells exposed to it. Metabolites such as acetate, produced by the microbiota, may affect the intracellular pool of acetyl coenzyme A that is used as a substrate for acetylating histones and thus regulating gene expression. This may also be an interesting topic of study in light of the ability of gut-resident T_{RM} to rejoin the systemic circulation and immune responses [55].

The major metabolic change we identified upon adaptation of $CD8^+$ T cells to the gut environment was a stark reduction in mitochondrial content driven by sensing of prostaglandin E_2 (PGE_2). We suggest that T cells clear mitochondria following a drop in mitochondrial membrane potential driven by PGE_2 and its regulation of the malate-aspartate shuttle. Despite mitochondrial depolarization and clearance, gut-resident T cells showed a viable energy balance and the remaining mitochondria could efficiently engage the electron transport chain. Our analysis did not show whether the entire mitochondrial repertoire of a cell was homogeneously affected by PGE_2. It is likely that depolarized *vs* polarized mitochondria are sorted for clearance through autophagy, and it would be interesting to study if and how mitochondria can be controlled at the single organelle level to ultimately support cell viability and function. It is also worth noting that cells in the gut showed a reduced ATP:AMP ratio, which may affect their long-term performance in coping with the continuously challenging environment of the gut.

Our metabolomic analysis of the interstitial fluid showed that in steady-state physiological conditions PGE_2 is present in the gut microenvironment and affects $CD8^+$ T cell mitochondrial content. PGE_2 has been widely recognized to affect several aspects of T cell immune responses and intestinal physiology [39, 56-60]. Indeed, PGE_2 is an integral component of the gut environment, essential to promote epithelial maintenance upon the constitutive stress posed by the microflora [39, 40]. While gut IEL have been shown to have reduced mitochondrial mass as well as a different proteome as compared to mLN-resident $CD8^+$ T cells [32, 61], our data establish a mechanistic link between physiological PGE_2 concentrations in the intestine and how they affect T cells to shape their metabolic profile and adaptation to the gut environment. It remains to be assessed how PGE_2 production is regulated in the gut and whether PGE_2 concentrations increase in other peripheral tissues upon pathological changes, such as described in the tumor microenvironment [62]. Similarly, as sensing of PGE_2 is affected by expression of EP receptors, the tissue-specific receptor expression likely influences the effect of PGE_2 in different cell types. Differently from $CD8^+$ T cells, gut-isolated macrophages did not reduce their mitochondrial content. While a subset of gut-resident macrophages, as well as other intestinal cells, was found to express *Ptger4* and/or other EP receptors [63-65], it is likely that additional factors play a role in shaping the mitochondrial content of gut-resident cells. For instance, we showed that the activation profile of macrophages could circumvent the mitochondrial changes driven by PGE_2 exposure [41]. While PGE_2 itself was found to trigger autophagy, this could also occur as a consequence of the PGE_2-driven mitochondrial depolarization. The binding of PGE_2 to EP4 engages the cAMP/PKA pathway, and it has been suggested that PGE_2 may directly activate PI3K [66], providing a potential explanation of the effect of the PI3K inhibitor wortmannin in preventing both mitochondrial clearance and reduction of mitochondrial membrane potential, as compared to bafilomycin A1, an inhibitor of late stages of autophagy, the effect of which is restricted to mitochondrial clearance. Our data implicating a role for autophagy in mitochondrial quality control of gut $CD8^+$ T cells are in line with findings that highlighted autophagy as a key pathway required for the establishment of $CD8^+$ T cell tissue residence [67]. In addition, while the mitochondrial fission-inducing protein DRP1 is required for mitophagy in cardiomyocytes [68], deletion of *Drp1* did not prevent the loss of mitochondrial mass observed upon entry of CD8$^+$ T cells in the intestine. It is possible that gut-adapting CD8$^+$ T cells use additional strategies beyond autophagy to clear mitochondria. For example, migratory cells are able to dispose of damaged mitochondria through a process called mitocytosis [69].

While deletion of the EP4 receptor promoted accumulation of CD8$^+$ T cells in the intestinal wall, tampering with autophagy or glutathione pathways negatively affected the establishment of the intestinal T cell pool, supporting a key role for these processes in regulating T cell function and intestinal homeostasis [46, 47, 70-73]. Of note, the teleology of our findings may appear peculiar, that is, why gut-resident CD8$^+$ T cells express a receptor (EP4) that hinders their fitness. It is however tempting to speculate that PGE$_2$ may play a role in 'updating' the intestinal CD8$^+$ T cell pool. By triggering mitochondrial dysfunction, and thus shortening the life span of the cells [74], PGE$_2$ may continuously remodel the CD8$^+$ T cell repertoire to adapt to ever-changing conditions, such as those presented by the microbiota or food antigens. Alternatively, PGE$_2$ sensing and the subsequent reduction of mitochondrial content in T cells, may represent one of the strategies in place in the gut to constrain the CD8$^+$ immune response mediated by T$_{EM}$. Our results seem to support this hypothesis as *Ptger4* deletion not only triggered accumulation of CD8$^+$ T cells in the gut, but also retained them in the CD69$^-$CD103$^-$ state. While autophagy is intrinsically required to clear the damaged mitochondria and preserve a viable size of the CD8$^+$ T cell compartment, elevated glutathione may be a consequence of the depolarization of mitochondria and elevated mitochondrial ROS driven by PGE$_2$, and could modulate its 'purging' effect on the T cell pool. In addition, our findings may aid in the interpretation of the counterintuitive clinical phenomenon of non-steroidal anti-inflammatory drug (NSAID)-induced colitis (NSAIDs are known inhibitors of PGE$_2$ biosynthesis), suggesting a possible role for the accumulation of CD8$^+$ T cells in driving the disease [75]. It is however worth noticing that under certain experimental settings, T cells have been shown to be dispensable for the induction of NSAID-triggered colitis [57]. Finally, our data showed that gut residency of CD8$^+$ T cells is characterized by reduced mitochondrial content, as well as by reduced levels of NAD$^+$, and a possibly diminished glycolytic flux. The origin of these phenomena likely lies in the effect of PGE$_2$ on the function of the malate-aspartate shuttle, causing the "cooling down" of CD8$^+$ T cell metabolism upon sensing the gut microenvironment, a hypothesis in line with recent literature showing limited metabolic activation of gut-resident T cells [76].

Immune checkpoint inhibitors (ICI) have thus far shown limited success in colorectal cancers (CRC, [77]). We speculate that mitochondrial loss in T cells could be an underlying factor contributing to the lack of efficacy of ICI in CRC. While exposure to PGE$_2$ does not appear to diminish T cell function, such as the production of IFN-γ, it nevertheless limits cell numbers in the niche. Moreover, recent data showed that inhibition of PGE$_2$ sensing by EP2 and EP4 receptors promoted accumulation of CD8$^+$ T cells within tumors [78]. Our data corroborate these findings by showing that EP4-deficient T cells outcompete wild type cells to occupy the intestinal niche in greater numbers, suggesting that pharmacological blockade of the PGE_2 receptor or PGE_2 synthesis might increase T cell numbers in the gut. We question whether combining ICI with PGE_2 pathway inhibition could enhance the outcome of ICI in CRC by increasing the number of $CD8^+$ T cells in the niche, as previously suggested [62]. Further, it is likely that ICI efficacy may require T cells to have 'fit' mitochondria, and not dysfunctional ones, as results from PGE_2 exposure. We speculate that the PGE_2-autophagy-glutathione pathway could be targeted to fine-tune the accumulation of $CD8^+$ T cells in the gut, to modulate immune responses underscoring inflammatory bowel disease and cancer.

In summary, we propose that a balance between PGE_2 sensing, mitochondrial clearance, and glutathione-regulated redox balance shapes the adaptation of $CD8^+$ T cells to the gut microenvironment and ultimately the establishment of the $CD8^+$ T cell pool. PGE_2 is required for gut epithelial stability and repair, therefore it is an integral part of this tissue's environmental signature. As T cells transition from the mLN to the gut wall, they become exposed to PGE_2. This causes mitochondrial depolarization and affects mitochondrial fitness. However, T cells adapt by engaging autophagy to clear depolarized mitochondria and augment glutathione synthesis to regulate cellular redox balance – these metabolic adaptations allow gut T cells to maintain function and carry on. Thus, we conclude that the environment surrounding $CD8^+$ T cells impinges on their metabolic choices, complements cytokine sensing and transcriptional rewiring, and allows T cells to adapt and function in the newly encountered tissue niche.

Methods

Mice, in vivo treatments and ethical statement

C57BL/6J mice (RRID: IMSR_JAX:000664), PhAM mice (RRID: IMSR_JAX:018397), CD4^{Cre} mice (RRID: IMSR_JAX:017336), Drp1^{floxed} mice (gift from Hiromi Sesaki), Great mice (interferon-γ reporter, RRID: IMSR_JAX:017580), major histocompatibility complex (MHC) class I-restricted ovalbumin (OVA)-specific TCR OT-I transgenic mice (RRID: IMSR_JAX:003831), CD45.1 congenic mice (RRID: IMSR_JAX:002014), Thy1.1 congenic mice (RRID: IMSR_JAX:000406) were purchased from The Jackson Laboratory. Mito-roGFP2-Orp1 mice (tracking mitochondrial H_2O_2 production) [44, 45] were a kind gift from Tobias P. Dick (DKFZ).

All mice were maintained in the animal facilities at the Max Planck Institute for Immunobiology and Epigenetics, under specific-pathogen free (SPF) conditions and following institutional animal use and care guidelines. Mice were exposed to a 14h/10h light/dark cycle and fed *ad libitum* with acidified water (pH 2.5-3.3). Euthanasia and animal procedures were conducted on 8-12 weeks old male and/or female mice, age-matched and sex-matched, in compliance to § 4, paragraph 3 of the German Animal Protection Act, animal licenses 35-9185.81/G-20/107 and 35-9185.81/G-20/101, approved by the Regierungspräsidium Freiburg.

To assess residency of T cells in various tissues, mice were injected intravenously (iv) with 2.5 µg of fluorescently labeled anti-CD45 antibody (clone 30-F11), 10 minutes before euthanasia, perfusion and analysis.

To establish the antigen-specific *Listeria monocytogenes* infection model, we proceeded as follows. 10^4 naive congenically-marked OT-I cells (CD90.1$^+$ in experiments in Figure 3d and f, CD45.2$^+$ in experiments in Figures 4, 5 and 6 and Extended Data Fig. 4-7) were adoptively transferred in unchallenged recipient CD90.2$^+$ CD45.1$^+$ mice. In the competition experiments shown in Figures 4-6, 10^4 or 10^5 (*Got1* experiments) naive congenically-marked OT-I cells (CD45.2$^+$ and CD90.2$^+$) and 10^4 or 10^5 (Got1 experiments) naive congenically-marked OT-I cells (CD45.2$^+$ CD90.1$^+$) were genetically modified by CRISPR-Cas9 (see details below) and co-transferred in unchallenged recipient CD45.1$^+$ mice. 24h after the adoptive transfer, recipient mice were challenged with 10^9 CFU of *LmOVA* intra-gastric (oral gavage, og). Mice were monitored daily, euthanized and analyzed 7 or 24 days post infection.

Isolation of cells

To isolate cells from the spleen and mesenteric lymph nodes (mLN), the organs were mashed on a 70 µm strainer in medium containing RPMI1640, 10% heat-inactivated fetal calf serum (FCS), 4 mM glutamine, 1% penicillin/streptomycin solution and 55 µM β-mercaptoethanol (hereafter named complete medium). Cell suspensions were treated with Gey's solution for 3 minutes if red blood cell lysis was required. Finally, cells were extensively washed and suspensions used for downstream applications. Purification of CD8$^+$ T cells for sorting or cell culture was performed using a mouse CD8$^+$ T cell isolation kit (Stem Cell Technologies, Cat# 19853), following the manufacturer's instructions.

Isolation of cells from the small intestine was performed as follows. Upon harvesting, fat tissue bordering the small intestine was carefully removed and Peyer's patches were excised. Small intestines were cut open, washed with ice cold PBS 1X + 25 mM Hepes, cut in 2 cm-long pieces and collected in medium containing RPMI1640, 25 mM Hepes, 3% FCS, 4 mM glutamine, 1% penicillin/streptomycin and 55 µM β-mercaptoethanol (hereafter named 3% FCS medium). Small intestines were incubated in 3% FCS medium added with 5 mM EDTA and 1 mM dithiothreitol (DTT) for 25 minutes, at 37 C, 5% CO_2 and agitation (1st incubation). After the incubation, cells in suspension were collected, consecutively strained through 100 µm and 40 µm strainers, washed and kept as intraepithelial lymphocyte (IEL) fraction. The leftover small intestine pieces were thoroughly (4 times) washed by shaking with ice cold medium containing RPMI1640, 25 mM Hepes, 4 mM glutamine, 1% penicillin/streptomycin and 55 mM β-mercaptoethanol (hereafter named serum-free medium) added with 2 mM EDTA. Washed small intestine pieces were then finely chopped and incubated in serum-free medium added with 100 µg/ml Liberase TL (Roche) and 50 µg/ml DNAse I (Roche) for 35 minutes, at 37 C, 5% CO_2 and agitation (2nd incubation). After digestion, suspensions were strained through 70 µm strainers, washed and kept as lamina propria (LP) fraction. LP and IEL were enriched for leucocytes using a three-layers percoll gradient (percoll 75%, 40% and 30%) centrifuged for 20 minutes, at room temperature, 680 g, without any centrifuge acceleration or brake. The leucocyte layer between percoll 75% and 40% was collected as enriched LP or IEL fraction, extensively washed and suspensions used for downstream applications. In some experiments, 1 µM of KN-62 (Sigma), inhibitor of P2RX7 used to limit cell death during intestine digestion [35], was added to media used in the 1st and 2nd incubation.

T cell isolation from the liver was performed as follows. Whole liver was collected in ice cold complete medium, finely chopped and incubated in RPMI1640 added with 1 mg/ml collagenase IA (Sigma) and 50 µg/ml DNAse I (Roche) for 45 minutes, at 37 C, 5% CO_2 and agitation. After digestion, suspensions were strained through 70 µm strainers, washed and enriched for leucocytes using percoll 33% and centrifuging them for 20 minutes, at room temperature, 680 g. The leucocyte pellet was collected, extensively washed, red blood cell lysis was performed and suspensions used for downstream applications.

Lung digestion was performed as follows. Lungs were collected in ice cold complete medium, finely chopped and incubated in complete medium added with 1 mg/ml collagenase IA (Sigma) and 50 µg/ml DNAse I (Roche) for 45 minutes, at 37 C, 5% CO_2 and agitation. After digestion, suspensions were strained through 70 µm strainers, washed and enriched for leucocytes using a three-layers percoll gradient (percoll 75%, 40% and 30%) centrifuged for 20 minutes, at room temperature, 680 g, without any centrifuge acceleration or brake. The leucocyte layer between percoll 75% and 40% was collected, extensively washed and suspensions used for downstream applications.

To isolate human PBMCs from fresh blood samples, blood was first diluted 1:1 with PBS 1X + 2% FCS. Samples were then layered in SepMate^{TM} PBMC isolation tubes (Stem Cell Technologies) preloaded with Lymphoprep (Stem Cell Technologies) and centrifuged for 10 minutes, at room temperature, 1200 g. The PBMC layer was collected and extensively washed in PBS 1X + 2% FCS and suspensions used for downstream applications.

For isolation of cell from human gut biopsies, we proceeded as follows. Fresh or frozen gut biopsies (5 mm; matched with fresh or frozen PBMCs) were mashed through 70 µm strainers in complete medium. Suspensions were extensively washed and finally used for downstream applications.

Fluorescence-Activated Cell Sorting (FACS)

To analyze the CD8$^+$ T cell response in humans we used the surface markers CD45RA, CD27, CD69 and CD103, identifying by flow cytometry five CD8$^+$ T cell populations: CD45RA$^+$CD27$^+$ T$_N$, CD45RA$^-$CD27$^-$ T$_{EM}$, CD45RA$^+$CD27$^-$ T$_{EMRA}$ and CD45RA$^-$CD27$^+$ T$_{CM}$ isolated from blood; CD69$^+$CD103$^+$ T$_{RM}$ isolated from gut biopsies. To analyze the continuum of the gut immune response in mouse we used the surface markers CD62L, CD44, CD69 and CD103, identifying by flow cytometry seven CD8$^+$ T cell populations that approximate the transition of CD8$^+$ T cells from mLN to the intestine: CD62L$^+$CD44$^-$ T$_N$, CD62L$^+$CD44$^+$ T$_{CM}$, CD62L$^-$CD44$^+$CD69$^-$CD103$^-$ T$_{EM}$ and CD62L$^-$CD44$^+$CD69$^+$CD103$^+$ T$_{RM}$ isolated from mLN; CD44$^+$CD69$^-$CD103$^-$ and CD44$^+$CD69$^+$CD103$^+$ from LP; and CD44$^+$CD69$^+$CD103$^+$ induced CD8$\alpha\beta$ T$_{RM}$ from IEL. Of note, it has been previously shown that acquisition of tissue residency drives sequential expression of CD69 and CD103, thus suggesting that LP-isolated CD69$^-$CD103$^-$ may qualify as recent emigrants from the blood about to transit towards the CD69$^+$CD103$^+$ phenotype [17].

Before staining with MitoTracker^{TM} Green or TMRM, cell suspensions were counted and equal cell numbers were stained to prevent uneven staining of suspensions with different cell numbers, and thus bias the analysis. The following dyes and staining procedures were used. MitoTracker^{TM} Green FM (Invitrogen) was used to stain cells at a concentration of 100 nM in complete medium, for 30 minutes, at 37 C, 5% CO_2. In some experiments, 50 µM of Verapamil (Sigma), inhibitor of mitochondrial efflux pumps encoded by *Bcrp1* and *Mdr1a/b*, used to prevent efflux of MitoTracker^{TM} green FM from mitochondria [34], was added to the staining medium. Tetramethylrhodamine methyl ester perchlorate (TMRM, Invitrogen) was used to stain cells at concentrations of 50 or 10 nM, according to the experiment, in complete medium, for 30 minutes, at 37 C, 5% CO_2. In experiments where TMRM kinetic was analyzed, 500 nM cyclosporin H (Sigma), another inhibitor of mitochondrial efflux pumps used to prevent efflux of TMRM from mitochondria, was added to the staining and acquisition media. In the same experiments, oligomycin (Sigma), inhibitor of complex V of the electron transport chain (ETC) was used at a concentration of 10 µM, whereas carbonilcyanide p-triflouromethoxy-phenylhydrazone (FCCP, an ionophore that permeabilize the inner mitochondrial membrane to H^+, Sigma) was used at a concentration of 10 µM. CellROX^{TM} Deep Red or Green (Invitrogen) was used to stain cells at a concentration of 250 nM in complete medium, for 30 minutes, at 37 C, 5% CO_2. In the experiments using Mito-roGFP2-Orp1 mice, gates were set upon treating the cells with the reducing agent DTT (10 mM, 15 mins) or the oxidizing reagent diamide (1 mM, 15 mins).

Cell viability was quantified by flow cytometry using LIVE/DEAD^{TM} blue or near-IR dyes (Invitrogen) or Zombie Green^{TM} dye (Biolegend), following manufacturer instructions.

Surface staining was performed in PBS 1X + 2% FCS + 5 mM EDTA, for 20 minutes, on ice, in the dark, upon blocking cells with anti-CD16/32 (clone: 93, Biolegend). The following antibodies (clone in brackets) were used for surface staining of murine cells: anti-CD45 (30-F11), anti-CD8α (53-6.7), anti-CD8β (53-5.8), anti-CD62L (MEL-14), anti-CD44 (IM7), anti-CD69 (H1.2F3), anti-CD64 (X54-5/7.1), anti-F4/80 (BM8), anti-Ly6G (1A8), anti-TIM4 [54(RMT4-54)], anti-CD45.2 (104), anti-Thy1.1 (OX-7) all from Biolegend; anti-CD103 (2E7), from Invitrogen; anti-Siglec F (E50-2440), from BD. The following antibodies (clone in brackets) were used for surface staining of human cells: anti-CD19 (HIB19), anti-CD3 (HIT3a), anti-CD8 (HIT8a), anti-CD69 (FN50), anti-CD103 (Ber.ACT8), anti-CD45RA (HI100), anti-CD27 (LG3A10), all from Biolegend.

Intracellular staining was performed upon restimulation of *ex vivo* isolated cells in U-bottom plates coated with anti-CD3 at 5 µg/ml and resuspending the cells in complete medium added with 100 U/ml IL-2 and soluble αCD28 at 0.5 µg/ml, in presence of brefeldin A 1:1000 (Biolegend), under 5% CO_2, atmospheric oxygen, at 37 C in a humidified incubator for 4h. After surface staining, intracellular staining was performed using Citofix/Cytoperm^{TM} kit (BD) following manufacturer instructions and using the following antibodies: anti-interferon γ (XMG1.2), anti-TNF (MP6-XT22), all from Biolegend

Cells were acquired on BD LSRFortessa^{TM} or BD FACSymphony^{TM}, or they were sorted using BD FACSAria^{TM}. Raw data were analyzed with FlowJo (BD).

TotalSeq^{TM} antibody staining

TotalSeq^{TM}-A Custom Mouse panel including 198 antibodies was obtained from Biolegend (#99833). The staining procedure was performed immediately after cell sorting and strictly following manufacturer instructions. Specifically, 25 µl of TotalSeq^{TM}-A antibody cocktail were used to label

25 µl of cell suspension containing 5×10^5 cells. 4 groups of samples have been prepared for TotalSeq^{TM}-A antibody staining and the following single cell RNA sequencing (scRNAseq), in biological triplicate: 1. naive and central memory $CD8^+$ T cells ($CD62L^+$) isolated from mLN (mLN T_N and T_{CM}); 2. effector memory $CD8^+$ T cells ($CD62L^-$ $CD44^+$) isolated from mLN (mLN T_{EM}); 3. total $CD8^+$ T cells isolated from LP (LP CD8); 4. total $CD8^+$ T cells isolated from IEL (IEL CD8). This strategy was designed to focus the analysis on $CD8^+$ T cells (hence the cell sorting approach), to monitor the entire course of the response (from mLN to IEL) and to enhance the resolution of the analysis to the stages involving the T cell adaptation to the intestinal tissue (hence the higher number of cells analyzed from LP).

Single cell RNA sequencing

After staining with TotalSeq^{TM}-A antibodies, suspensions were used for single cell RNA sequencing (scRNAseq), hereafter briefly described. Following the protocol CG000204 RevD from 10X Genomics, we aimed at analyzing 1,000 cells of group 1 (mLN T_N and T_{CM}), 5,000 cells of group 2 (mLN T_{EM}), 10,000 cells of group 3 (LP CD8) and 5000 cells of group 4 (IEL CD8). At step 2.2, we followed Biolegend instructions to add ADT additive primers. Step 2.3 (and only this step) was performed following the protocol CG000185 RevD from 10X Genomics. 3' gene expression libraries were further processed following the protocol CG000204 RevD from 10X Genomics, whereas ADT libraries (cell surface protein libraries) were processed following instructions from Biolegend. 3' gene expression and ADT libraries were quantified by fragment analyzer and pooled for multiplexed sequencing on a NovaSeq 6000 instrument by the Deep-sequencing Facility at the Max Planck Institute for Immunobiology and Epigenetics. 3' gene expression libraries were run with a read length of 2x100 whereas ADT libraries were run with a read length of 2x50. Both libraries were sequenced using the following parameters, as recommended by 10X Genomics and Biolegend: Read 1: 28 cycles, i7: 8 cycles, i5: 0 cycles, Read 2: 91 cycles. 50,000 reads/cell were sequenced for 3' gene expression libraries, 12,500 reads/cell were sequenced for ADT libraries.

Samples were demultiplexed and aligned using Cell Ranger 6.1 (10X Genomics) to genome build mm10 to obtain a raw read count matrix of barcodes corresponding to cells and features corresponding to detected genes. Read count matrices were processed, analyzed and visualized in R v. 4 (R Core Team 2013) using Seurat v. 4 [79] with default parameters in all functions, unless specified. Poor quality cells, with low total unique molecular identifier (UMI) counts (< 4,000), low number of detected genes (< 1,500) and high percent mitochondrial gene expression (> 20%), were excluded. Filtered samples were normalized using a regularized negative binomial regression (SCTransform) [80] and merged. Principal component analysis was performed on merged matrices and the first 50 principal components were used for downstream analysis. Integrated gene expression matrices were visualized with a UMAP (McInnes et al. 2018; arXiv:1802.03426) as a dimensionality reduction approach. For ADT libraries, samples were demultiplexed and then processed with CITE-seq-Count v. 1.4.5 (Roelli, P et al. 2019). Later merged and harmonized to remove biological replicate associated effects using harmony [81]. A combined UMAP for RNA and ADT profiles was generated by building a weighted nearest neighbors graph based on their respective PCA projections [79]. Resolution for cell clustering was determined by evaluating hierarchical clustering trees at a range of resolutions (0-1.2) with Clustree [82], selecting a value inducing minimal cluster instability. Differentially expressed genes between clusters were identified as those expressed in at least 25% of cells with a greater than +0.5 $\log_{10}$ fold change and an adjusted *p* value of less than 0.01, using the FindMarkers function in Seurat v.4 with all other parameters set to default. Ribosomal protein genes were excluded from results. Cluster specific genes were explored for pathway enrichment using Biological Process Gene Ontology annotation with goseq v. 1.40.0 [83]. Gene set scores were calculated using the AddModuleScore function in Seurat v.4 with default parameters. Briefly, the average expression levels of each identified gene set were calculated on a single cell level and subtracted by the aggregated expression of randomly selected control gene sets. For this purpose, target genes are binned based on averaged expression, and corresponding control genes are randomly selected from each bin. Cell trajectories and pseudotime estimations were calculated with Slingshot v. 1.6.1 [33], using UMAP projection and pre-calculated clustering as input for getLineages and getCurves functions with default parameters, setting origin to cluster 6. Trajectory dependent gene regulation was visualized by fitting general additive models [77] using gam v. 1.20 (Hastie, T 2020) using locally estimated scatterplot smoothing (loess) smooth terms.

Western blot

For western blotting analysis, cells were washed with ice cold PBS 1X and lysed in 1X Cell Signaling lysis buffer (20 mM Tris-HCL [pH 7.5], 150 mM NaCl, 1 mM Na_2EDTA, 1mM EGTA, 1% Triton X-100, 2.5 mM sodium pyrophosphate, 1 mM β-glycerophosphate, 1mM Na_3VO_4, 1 µg/mL leupeptin), supplemented with 1X Protease Inhibitor Cocktail (Cell Signaling, #5871) for 30 min, on ice, followed by centrifugation at 12,000 g for 10 minutes, at 4 C. Cleared protein extracts were denatured with NuPAGE^{TM} LDS loading buffer (Invitrogen) added with 50 mM DTT for 10 min at 75 C and loaded onto precast NuPAGE^{TM} 4-12% bis-tris protein gels (Invitrogen), or NuPAGE^{TM} 12% bis-tris protein gels (these ones were used for LC3 immunoblotting, Invitrogen). Samples were loaded according to the cell number: Between $5x10^4$ and $2x10^5$ cells per sample were analyzed, normalizing the loading within every experiment. Protein samples were run using MES buffer 1X (Invitrogen). Proteins were transferred onto nitrocellulose membranes using the iBLOT2 system (Invitrogen) following the manufacturer protocols. Membranes were blocked for 1h with 5% w/v milk in TBS 1X added with Tween-20 0.05% and incubated with primary antibodies in 5% w/v milk in TBS 1X added with Tween-20 0.05% overnight at 4 C or 1h at room temperature. The following primary antibodies were used: anti-TOM20 (clone D8T4N, 1:1,000, Cell Signaling), anti-TFAM (polyclonal, 1:1,000, Abcam), anti-β actin (clone 13E5, 1:10,000, Cell Signaling), anti-OPA1 (clone 18/OPA-1, 1:2,000, BD), anti-EP4 (encoded by *Ptger4*, clone C-4, 1:100, Santa Cruz), anti-ATG5 (clone D5F5U, 1:1,000, Cell

Signaling), anti-Gclc (clone OTI1A3, 1:1,000, Invitrogen), anti-LC3B (polyclonal, 1:3,000, Sigma), anti-SQSTM1/p62 (clone D1Q5S, 1:1,000, Cell Signaling), anti-Got-1 (clone E4A4O, 1:1,000, Cell Signaling). All primary antibody incubations were followed by incubation with secondary HRP-conjugated antibodies (Pierce) in 5% w/v milk in TBS 1X added with Tween-20 0.05% for 1h at room temperature and visualized using SuperSignal West Pico or Femto Chemiluminescent Substrate (Pierce) using Biomax MR Film (Kodak) or a Bio-Rad ChemiDoc^{TM} Imaging System. Optical density of the signals on the film was quantified using grayscale measurements in ImageJ software (NIH) and converted to fold change, normalized to the loading control.

Fluorescence microscopy

Spinning disk confocal imaging was performed as follows. Cells were isolated and sorted as previously described from unchallenged PhAM mice. A minimal surface staining panel was used for sorting the cells to minimize interference with the PhAM signal during spinning disk acquisition. After sorting, cells were resuspended in complete medium and transferred to Lab-Tek^{TM} II chambers (Nunc) coated with poly-D-lysine. Chambers were spun to favor attachment of the cells to the bottom of the chambers. During the entire experiment, cells were maintained alive at 37 C, 5% CO_2 using a Tokai Hit chamber. Fluorescence of Dendra2 (fluorescent protein in PhAM mice) and Hoechst 33342 (nuclear counterstaining) was acquired using a Zeiss spinning disk confocal with an Evolve (EMCCD) camera. Confocal images were deconvoluted using Huygens software and analyzed using Imaris imaging software.

Transmission electron microscopy

Between 2.5 x 10^5 and 10^6 cells were processed for electron microscopy. After FACS sorting, cells were fixed in glutaraldehyde 2.5% in 0.1 M sodium cacodylate buffer pH 7.4, for 20' at RT, washed in the same buffer, and stored at +4C until analysis.

Bulk RNA sequencing

For bulk RNA sequencing, 10^5 cells per target population from each of 3 biological replicates were isolated, processed and analyzed. RNA was extracted using RNAqueous^{TM} Total RNA isolation kit (Ambion) according to manufacturer instructions and quantified using Qubit 2.0 (Thermo Fisher Scientific) following manufacturer instructions. Libraries were prepared using the NEBNext Single Cell/Low Input RNA Library Prep Kit for Illumina and sequenced with a NovaSeq 6000 instrument by the Deep-sequencing Facility at the Max Planck Institute for Immunobiology and Epigenetics. Sequenced libraries were processed with deepTools [84, 85], using STAR [86], for trimming and mapping, and featureCounts [87] to quantify mapped reads. Raw mapped reads were processed in R (Lucent Technologies) with DESeq2 [88], to determine differentially expressed genes (adjusted p value < 0.05, $\log_2$ fold change > 1) and generate normalized read counts to be visualized as heatmaps using Morpheus (Broad Institute).

Human samples and ethical statement

Blood and intestinal tissue were collected after obtaining the written consent of all study participants and following approval of the Institutional Review Boards (Ethics Committee of the Albert Ludwigs University, Freiburg; #407/16 and #14/17). The study was performed in agreement with the principles expressed in the Declaration of Helsinki (2013).

Isolation of interstitial fluid

For isolation of tissue interstitial fluid we proceeded as follows adapting an already published protocol [89]. Upon perfusion with ice cold PBS 1X, tissues (spleen, mLN, small intestine, liver and lungs) were carefully excised to maintain their integrity and collected in ice cold PBS 1X. Blood was withdrawn by cardiac puncture and maintained on ice in absence of anticoagulants. Fecal content was collected from the lumen of the ileum section of the small intestine and kept on ice. Coagulated blood was spun for 10 minutes, 5,000 g, at 4 C and serum was collected and kept on ice until further processing. Fecal content was spun for 10 minutes, 400 g, at 4 C and supernatant was collected and kept on ice until further processing. Tissues were gently tapped on adsorbing paper, wrapped in a 20 μm nylon mesh and placed in a 1.5 ml tube. Tubes were centrifuged for 5 minutes, 70 g, 4 C to remove leftover PBS 1X. Tissue wrapped in the nylon mesh were transferred to another 1.5 ml tube and centrifuged for 10 minutes, 400 g, 4 C. The flow-through is tissue interstitial fluid and volumes between 1 and 15 μl were collected. Interstitial fluid was kept on ice until further processing.

Metabolomic analysis

Untargeted metabolomic analysis of interstitial fluid was performed as follows. 9 volumes of ice cold methanol 100% were added to the interstitial fluid, the samples vortexed and cooled on dry ice. Samples were centrifuged for 3 minutes, 20,000 g, at -9 C. Supernatant was collected and samples were stored at -80 C until further processing following protocols previously described [90]. Metabolites were analyzed and identified by fragmentation and retention time using Metaboscape software (Bruker).

Targeted metabolomic analysis was performed as follows. After sorting, $2x10^5$ cells were resuspended in complete medium and rested for 30 minutes at 37 C, 5% CO_2. Cells were washed in ice cold 3% glycerol and the pellet resuspended in extraction solution (ice cold 80% methanol). Samples were incubated for 5 minutes on ice and centrifuged for 3 minutes, 20,000 g, at -9 C. Supernatant was collected and kept on dry ice. Cell pellets were further resuspended for two more times with extraction solution and treated as previously described to further collect supernatants. Samples were finally dried using a Genevac EZ2 speed vac and stored at -80 C until further processing following protocols previously described [90]. Targeted metabolite quantification by LC-MS was carried out using an Agilent 1290 Infinity II UHPLC in line with an Agilent 6495 QQQ-MS operating in MRM mode. MRM settings were optimized separately for all compounds using pure standards. LC separation was on a Phenomenex Luna propylamine column (50 x 2 mm, 3 µm particles) as described previously [90]. Briefly, a solvent gradient of 100% buffer B (5 mM ammonium carbonate in 90% acetonitrile) to 90% buffer A (10 mM NH_4 in water) was used. Flow rate was from 1,000 to 750 µL/min. Autosampler temperature was 5 C and injection volume was 2 µL. Raw data were analyzed using the R package automRm [91]. Further analysis was performed using MassHunter software (Agilent).

In vitro T cell culture and treatments

Isolated $CD8^+$ T cells from OT-I mice were maintained in the naive status after CRISPR-Cas9 gene targeting by resting them overnight in complete medium added with IL-7 (Peprotech) at 10 ng/ml. Isolated T cells were otherwise activated using plate bound anti-CD3 (5 µg/ml, inVIVOMAb Cat# BE0002) in complete medium added with 100 U/ml IL-2 (Peprotech) and soluble αCD28 (0.5 µg/ml, inVivoMab Cat# BE0015) under 5% CO_2, atmospheric oxygen, at 37 C in a humidified incubator. At day 2 post activation, and then daily up to day 6, media were refreshed and cells counted and replated at a density of 10^6 cells/ml [for (IL-2)-T cells] or $1.5x10^6$ cells/ml [for (IL-15/TGF-β)-T cells]. (IL-2)-T cells were maintained in 100 U/ml IL-2 throughout the culture; to generate (IL-15/TGF-β)-T cells, cells were cultured in 10 ng/ml IL-15 and 10 ng/ml TGFβ starting from day 3 post-activation. Where indicated cells were treated with vehicle control (0.1% ethanol), PGE_2 (Sigma) at the indicated concentrations and for the indicated time, PGE_1 (Sigma), $PGF_{2\alpha}$ (Sigma), PGI_2 sodium salt (Sigma) and 15-deoxy-Δ12-14 PGJ_2 (Sigma) at 100 nM, bafilomycin A1 (Sigma) at 100 nM, Wortmannin (PI3K inhibitor, Selleckchem) at 10 µM and SBI-0206965 (ULK1 inhibitor, Sigma) at 2 µM.

CRISPR-Cas9 gene targeting

The following gRNA were used to target the genes *Ptger4*, *Atg5*, *Gclc* and *Got1* in naive $CD8^+$ T cells: *Ptger4* (Mm.Cas9.PTGER4.1.AA; Mm.Cas9.PTGER4.1.AG), *Atg5* (Mm.Cas9.ATG5.1.AA; Mm.Cas9.ATG5.1.AB), *Gclc* (Mm.Cas9.GCLC.1.AC; Mm.Cas9.GCLC.1.AD), *Got1* (Mm.Cas9.GOT1.1.AB; Mm.Cas9.GOT1.1.AD). The following guide was used as non-targeting control: Mm.Cas9.GCGAGGTATTCGGCTCCGCG. All guides were purchased from IDT.

To prepare the targeting gRNA-Cas9 complex, equimolar amounts (180 pmol) of Alt-R CRISPR-Cas9 tracrRNA (IDT) and gene-specific crRNA (indicated above) were mixed, incubated 5 minutes at 98 C and cooled at room temperature for 20 minutes. 60 pmol of recombinant Cas9 (IDT) was mixed and incubated for 20 more minutes. $5\text{-}10x10^6$ naive $CD8^+$ T cells isolated from OT-I mice were electroporated using the P4 Primary Cell 4D-Nucleofector^{TM} X Kit and the prepared gRNA-Cas9 complexes. After electroporation cells were recovered in complete medium added with components from the P4 Primary Cell 4D-Nucleofector^{TM} X Kit and 10 ng/ml of IL-7, overnight, at 37 C, 5% CO_2. Cells were then counted and further used for downstream applications.

Glutathione quantification

For glutathione quantification, 10^5 cells per target population were sorted and kept on ice until further processing using GSH-Glo^{TM} Glutathione Assay (Promega), strictly following manufacturer instructions. 1 mM Tris(2-carboxyethyl)phosphin-hydrochlorid (TCEP) was used when appropriate to reduce GSSG to GSH, differentially quantify GSSG, and ultimately calculate the GSH/GSSG ratio.

Statistical analysis

Comparisons between two groups were performed using unpaired or paired, two-tailed, Student’s *t* test. Comparisons between more than two groups were performed using one-way or two-way ANOVA and Tukey’s, Sidak's or Dunnet's multiple comparison test according to the experimental settings. Statistical significance is expressed throughout the text as precise *p* value. Statistical analysis was performed using Graphpad Prism 7 Software.

Statistical analysis of untargeted metabolomic data was performed applying a Student's *t* test between respectively: 1. metabolites identified in the small intestine and 2. metabolites identified in all the other tissues. This analysis was used to identify metabolites specifically present in the small intestine tissue. Analysis was performed using Metaboscape software (Bruker).

Further details on the statistical analysis can be found in the figures and the respective figure legends.

Acknowledgements

We thank current and past members of the Department of Immunometabolism at the Max Planck Institute for Immunobiology and Epigenetics (MPI-IE) for advice and discussions throughout the project. We specially thank Katharina Borst for critical reading of the manuscript. We thank Andrea Quintana and John Sutherland for their technical support, and the Flow Cytometry, Metabolomics, Microscopy, Deep Sequencing, and Animal Facility Cores, as well as the veterinarian and animal welfare officers at the MPI-IE. We thank Federico Caicci and Francesco Boldrin of the Electron Microscopy Lab at the University of Padova for expert processing of samples. This work was supported by the Max Planck Society, the Leibniz Prize (DFG), and AI156274 from the N.I.H. (to E.L.P.), the Fritz Thyssen Stiftung für Wissenschaftsförderung (to M.V.), an Alexander von Humboldt Postdoctoral Fellowship (to M.V.), and the Medical University of Graz. R.Z. was supported by the Deutsche Forschungsgemeinschaft – SFB-1479 – Project ID: 441891347. B.B. and E.J.P. were supported by the Deutsche Forschungsgemeinschaft – IMPATH-SFB – Project ID: 256073931.

Author information

Study design: MV.
Conceptualization, project insight, and data interpretation: MV, ELP, MC, DES.
Performing and analyzing experiments: MV, DES, PA, MC, AMK, CC, AR, GEC, NR, KMG, JC, FS, AH, FH, DJP.
Providing advice and materials: MAS, FB, AMK, A-MG, BK, NC-W, PH, BB, RZ, S, JMB, EJP.
Manuscript writing: MV, ELP.
Funding: ELP, MV.

Ethics Declarations

ELP and EJP are founders of Rheos Medicines. ELP is a SAB member of Immunomet Therapeutics. The other authors have declared that no competing interests exist regarding this manuscript**.**

Figure legends

Figure 1. The transcriptional and surface profiles of CD8$^+$ T cells undergo step-wise changes throughout the intestinal immune response under homeostatic conditions.

a. Schematic representation of the gut-specific CD8$^+$ T cell response and strategy designed to investigate it. Image created with Biorender.com.

b. Uniform Manifold Approximation and Projection (UMAP) of the single cell RNA and ADT sequencing data obtained from the experiments designed as in *A*. Upon clustering analysis, 10 RNA-based clusters (0-9) were identified, using a resolution of 0.2. 49,111 cells obtained from 4 tissues and 3 biological replicates were analyzed. Color-coding is indicated in the legend.

c. Heatmap showing the top 5 DEGs in each cluster. Every row in heatmap corresponds to a gene, every column to a cell. Color coding: orange, high expression; purple, low expression.

d. Heatmap showing the top 5 ADTs in each cluster. Every row in heatmap corresponds to a surface protein, every column to a cell. Color coding: orange, high expression; purple, low expression.

e. UMAP of the single cell RNA sequencing data. Color-coding is according to the tissue of origin as outlined in the legend. The labeling in quotation marks refers to the data in *b*.

f. Bar graph of the distribution of the clusters identified in *b* across different tissues of origin. Within every tissue, cell numbers are normalized to 100% and the fractional contribution of every cluster is indicated. Color-coding resembles the one used in *b*.

Figure 2. CD8$^+$ T cells entering the gut have remodeled the transcription of mitochondria-encoded genes.

a. UMAP of the single cell RNA and ADT sequencing data showing the ratio of mitochondrial transcripts over the total transcriptome, across different clusters. The labeling in quotation marks refers to the data in *figure 1b*. Violin plots show the fraction of mitochondria-derived transcripts over the total transcriptome, across different clusters. The black dashed line indicates the median value identified for cluster 6.

b. Plots representing the expression of selected genes as a function of pseudotime, as identified in the data shown in *Figure 1g*. On the x axis, the interquartile range of every cluster is indicated, to facilitate the correlation between gene expression and progression of cells through pseudotime. Color-coding is indicated in the legend.

c. UMAP of the single cell RNA and ADT sequencing data showing expression of selected genes across different clusters. The labeling in quotation marks refers to the data in *figure 1b*.

Figure 3. Gut-resident T cells have reduced mitochondrial content.

a. Flow cytometry analysis of Mitotracker green staining in the indicated cell populations isolated from blood and intestine of healthy humans. Lines in the dot plot show mean values and data represent n = 5 independent experiments. Statistics were performed using one-way ANOVA and Tukey's multiple comparison correction.

b. Flow cytometry analysis of Mitotracker green staining in the indicated cell populations isolated from mLN and intestine of unchallenged C57BL/6J mice. Dot plot shows the fraction of cells included in the gate showed in the histogram plot. Color-coding is as per legend. Lines in the dot plot show mean values and data represent n = 9 independent experiments. Statistics were performed using one-way ANOVA and Tukey's multiple comparison correction.

c. Western blotting analysis of Tom20 and TFAM in the indicated cell populations. The data shown are representative of n = 6 independent experiments.

d. Flow cytometry analysis of Mitotracker green staining in the indicated antigen-specific (CD90.1$^+$, white), and polyclonal (CD90.1$^-$, black) cell populations isolated from mLN and intestine of C57BL/6J mice orally challenged with *LmOVA* and analyzed 7 days post-infection. Lines in the dot plot show mean values and data represent n = 4 independent experiments. Statistics were performed using one-way ANOVA and Tukey's multiple comparison correction.

e. Flow cytometry analysis of TMRM staining in the indicated cell populations. Dot plot shows the fraction of cells included in the gate showed in the histogram plot (TMRM^{high} cells). Color-coding is as per legend. Lines in the dot plot show mean values and data represent n = 5 independent experiments. Statistics were performed using one-way ANOVA and Tukey's multiple comparison correction.

f. Flow cytometry analysis of TMRM staining in the indicated antigen-specific (CD90.1$^+$, white), and polyclonal (CD90.1$^-$, black) cell populations isolated from mLN and intestine of C57BL/6J mice orally challenged with *LmOVA* and analyzed 7 days post-infection. Lines in the dot plot show mean values and data represent n = 4 independent experiments. Statistics were performed using one-way ANOVA and Tukey's multiple comparison correction.

g. Flow cytometry analysis of kinetic TMRM staining in the indicated cell populations upon treatment with oligomycin and FCCP. TMRM was used at a concentration of 10 nM during the staining step. TMRM values are shown normalized to the baseline (before oligomycin treatment) of TMRM staining of the respective population. Color-coding is as per legend. Data are representative of n = 3 independent experiments.

h. Mass spectrometry analysis of AMP, ADP, ATP and ATP:AMP ratio in the indicated cell populations. The bars show mean ± SEM. Data show n = 3 independent experiments analyzed simultaneously. Statistics were performed using one-way ANOVA and Tukey's multiple comparison correction.

i. Flow cytometry analysis of the intracellular expression of interferon-γ protein (IFN-γ) in cell populations isolated from mLN and intestine of unchallenged GREAT mice (IFN-γ reporters). Lines in the dot plots show mean values and data represent n = 2 independent experiments.

Figure 4. Prostaglandin E_2 regulates mitochondrial content of gut-resident $CD8^+$ T cells.

a. Flow cytometry analysis of Mitotracker green staining in $CD8^+$ $CD69^+CD103^{+/-}$ cells isolated from the indicated tissues of unchallenged mice. Color-coding is as per legend. Lines in the dot plot show mean values and the data are representative of n = 2 independent experiments. Statistics were performed using one-way ANOVA and Tukey's multiple comparison correction.
b. Volcano plot shows the differential distribution of metabolites isolated from the interstitial fluid of different tissues. Dashed lines indicate the fold change filter of FC > 2 and FC < -2 and the *p*-value filter of p=0.05. Plot shows cumulative data of n = 4 independent experiments.
c. Bar graph shows the relative abundance of PGE_2 in interstitial fluid isolated from the indicated tissues. Graph shows mean values ± SEM of cumulative data of n = 4 independent experiments. Statistics were performed using one-way ANOVA and Tukey's multiple comparison correction.
d. Flow cytometry analysis of Mitotracker green and TMRM staining in $CD8^+$ T cells isolated from C57BL/6J mice and activated in T_{RM} polarizing conditions for 5 days and treated for 24 hours with 10 μM PGE_2. Lines in the dot plot show mean values and the data represent n = 3 independent experiments. Statistics were performed using two-tailed Student's *t* test.
e. Flow cytometry analysis of Mitotracker green and TMRM staining in $CD8^+$ T cells activated in T_{RM} polarizing conditions for 5 days and treated for 24 hours with 100 nM of different prostaglandins. Lines in the dot plot show mean values and the data are representative of n = 2 independent experiments. Statistics were performed using one-way ANOVA and Dunnet's multiple comparison correction.
f. UMAP of the single cell RNA and ADT sequencing data showing expression across different clusters of *Ptger4*.
g. Schematic representation of the antigen-specific *Listeria monocytogenes* infection model used in *Figures 4-5*. OT-I donor mice are used to isolated cells to respond to *LmOVA*. Donor cells are labeled with the surface antigen CD45.2, whereas recipient mice are congenic for the surface antigen CD45.1. To additionally separate control guide- *vs* target gene guides-treated donor cells, we employed the markers CD90.1 and CD90.2. Oral gavage administration of *LmOVA* was used to engage the gut-specific immune response. Image created with Biorender.com
h, i. Flow cytometry analysis of the distribution of Ctrl vs *Ptger4*-deleted $CD8^+$ T cells within the population of $CD45.2^+$ cells upon *LmOVA* challenge in LP (*h*) and IEL fraction (*i*). Lines in the dot plot show pairing within single mice, and the dot plots show cumulative data of n = 3 independent experiments. Statistics were performed using two-tailed paired *t* test.
j. Flow cytometry analysis of Mitotracker green staining in Ctrl vs *Ptger4*-deleted $CD69^+CD103^+$ cells isolated from LP of mice orally challenged with *LmOVA*. Lines in the dot plot show pairing within

single mice, and dot plots show cumulative data of n = 3 independent experiments. Statistics were performed using two-tailed paired *t* test.

k. Flow cytometry analysis of the distribution of Ctrl vs *Ptger4*-deleted CD8$^+$ T cells gated in the population of CD45.2$^+$ cells between CD69$^-$CD103$^-$, CD69$^+$ and CD69$^+$CD103$^+$ populations, upon *LmOVA* challenge in LP. Lines in the dot plot show mean values; dot plots show cumulative data of n = 3 independent experiments. Statistics were performed using two-way ANOVA and Sidak's multiple comparison correction.

Figure 5. Autophagy and glutathione maintain the fitness of gut-resident T cells.

a. Heatmaps show the expression of selected genes of bulk RNA sequencing data obtained from the indicated cell populations. Color-coding is as per legend (white, low expression; blue, high expression) and shows relative values within each gene. Data show n = 3 independent experiments.

b. Western blotting analysis of LC3 isoform distribution and p62 in the indicated cell populations. The data represent n = 2 independent experiments.

c. Transmission electron microscopy of the indicated cell populations isolated from unchallenged C57BL/6J mice. Yellow arrowheads indicate double membrane structures characteristic of autophagosomes. The panel show representative images of n = 1 experiment.

d. Flow cytometry analysis of Mitotracker green and TMRM staining in CD8$^+$ T cells isolated from C57BL/6J mice, activated in (IL-15/TGF-β)-T cells polarizing conditions for 5 days and treated with PGE$_2$ in presence of the autophagy inhibitor bafilomycin A1. Lines in the dot plot show mean values ± SEM and the data are representative of n = 5 independent experiments. Statistics were performed using one-way ANOVA and Tukey's multiple comparison correction.

e, f. Flow cytometry analysis of the distribution of Ctrl vs *Atg5*-deleted CD8$^+$ T cells within the population of CD45.2$^+$ cells upon *LmOVA* challenge in LP (*e*) and IEL fraction (*f*). Lines in the dot plot show pairing within single mice, and the dot plots show cumulative data of n = 3 independent experiments. Statistics were performed using two-tailed paired *t* test.

g. Flow cytometry analysis of Mitotracker green staining in Ctrl vs *Atg5*-deleted CD69$^+$CD103$^+$ cells isolated from LP of mice orally challenged with *LmOVA*. Lines in the dot plot show pairing within single mice, and dot plots show cumulative data of n = 3 independent experiments. Statistics were performed using two-tailed paired *t* test.

h. Flow cytometry analysis of the mitochondrial oxidative state, as indicated by a shift from green to blue fluorescence, in the indicated cell populations isolated from mLN and intestine of unchallenged Mito-roGFP2-Orp1. Lines in the dot plot show mean values and the data represent n = 2 independent experiments. Statistics were performed using one-way ANOVA and Tukey's multiple comparison correction.

i. Flow cytometry analysis of CellROX staining in the indicated cell populations. Lines in the dot plot show mean values and the data are representative of n = 3 independent experiments. Statistics were performed using one-way ANOVA and Tukey's multiple comparison correction.

j. Heatmaps showing the expression of selected genes of bulk RNA sequencing data obtained from the indicated cell populations. Color-coding is as per legend (white, low expression; blue, high expression) and is showing relative values within each gene. Data show n = 3 independent experiments.

k. Mass spectrometry analysis of levels of GSH and GSSG in the indicated cell populations. The bars show mean ± SEM. Data show n = 3 independent experiments analyzed simultaneously. Statistics were performed using one-way ANOVA and Tukey's multiple comparison correction.

l, m. Flow cytometry analysis of the distribution of Ctrl vs *Gclc*-deleted CD8$^+$ T cells within the population of CD45.2$^+$ cells upon *LmOVA* challenge in LP (*l*) and IEL fraction (*m*). Lines in the dot plot show pairing within single mice, and the data are representative of n = 2 independent experiments. Statistics were performed using two-tailed paired *t* test.

Figure 6. Got1 links PGE$_2$ with the regulation of mitochondrial content in intestinal CD8$^+$ T cells

a. Western blot analysis of LC3-I (non-lipidated) and LC3-II (lipidated) in (IL-15/TGF-β)-T cells cultured for 6 days and treated for 24h with or without 100 nM PGE$_2$. The dot plot shows quantification by densitometry. Lines in dot plots show mean values. Dot plots show cumulative data of n = 2 independent experiments. Statistics were performed using two-tailed paired *t* test.

b. Flow cytometry analysis of cell numbers of the indicated CD8$^+$ T cells subsets in mLN, LP and IEL of unchallenged *Drp1$^{fl/fl}$CD4Cre$^+$* and *Drp1$^{fl/fl}$CD4Cre$^-$* mice. Color-coding is as per legend. Lines in the dot plot show mean values and the data are representative of n = 2 independent experiments.

c, d. Flow cytometry analysis of Mitotracker green and TMRM staining in the indicated cell populations isolated from mLN and intestine of unchallenged *Drp1$^{fl/fl}$CD4Cre$^+$* and *Drp1$^{fl/fl}$CD4Cre$^-$* mice. Color-coding is as per legend in panel *b*. Lines in the dot plot show mean values and the data are representative of n = 3 independent experiments.

e. Heatmaps show the expression of *Got1* in bulk RNA sequencing data obtained from the indicated cell populations. Color-coding is as per legend (white, low expression; blue, high expression) and shows relative values within the *Got1* gene. Data show n = 3 independent experiments.

f. UMAP of the single cell RNA and ADT sequencing data showing expression across different clusters of *Got1*.

g. Mass spectrometry quantification of NAD$^+$ in the indicated cell populations. The bars show mean ± SEM. Data show n = 3 independent experiments analyzed simultaneously. Statistics were performed using one-way ANOVA and Tukey's multiple comparison correction.

h, i. Flow cytometry analysis of Mitotracker green (*h*) and TMRM (*i*) staining in Ctrl vs *Got1*-deleted CD69$^-$CD103$^-$, CD69$^+$ and CD69$^+$CD103$^+$ cells isolated from LP of mice orally challenged with *LmOVA*. Lines in the dot plot show pairing within single mice, and dot plots show cumulative data of n = 2 independent experiments. Statistics were performed using two-way ANOVA and Sidak's multiple comparison correction.

j. Flow cytometry analysis of the distribution of Ctrl vs *Got1*-deleted CD8$^+$ T cells gated in the population of CD45.2$^+$ cells between CD69$^-$CD103$^-$, CD69$^+$ and CD69$^+$CD103$^+$ populations, upon *LmOVA* challenge in LP. Lines in the dot plot show pairing within single mice; dot plots show cumulative data of n = 2 independent experiments. Statistics were performed using two-way ANOVA and Sidak's multiple comparison correction.

k. After activation of CD8$^+$ T$_N$ in the mLN, CD8$^+$ T cells migrate and enter the intestinal wall. Here, they sense PGE$_2$ via the EP4 receptor. PGE$_2$ drives reduction of mitochondrial membrane potential, in part via alteration of the malate-aspartate shuttle, and ultimately leads to drop of mitochondrial mass. Autophagy contributes to the clearance of depolarized mitochondria, whereas glutathione maintains the redox balance by scavenging mitochondrial ROS, to ultimately shape the pool of gut-resident CD8$^+$ T cells.

Extended Data

Extended Data Figure 1. Single cell RNA sequencing reveals the dynamics of the intestinal immune response under homeostatic conditions.

a. Representative flow cytometry plots to show the sorting strategy of the experiments designed in *Figure 1*. Cells were sorted from the T_N and T_{CM} and T_{EM} gates of mLN, CD8$^+$ T gates of LP and IEL.
b. Dot plot showing the fraction of CD8$^+$ T cells localized in the vasculature at the time of isolation from the indicated tissues. Data were obtained by intravascular staining with anti-CD45 antibody. Data from 1 experiment.
c. UMAP of the single cell RNA and ADT sequencing data obtained from the experiments designed as in *Figure 1*. Color-coding is according to the biological replicate as outlined in the legend. The bar graph shows the distribution of the analyzed cells in every cluster across the biological replicates.

Extended Data Figure 2. Adaptation of CD8$^+$ T cells to the gut microenvironment correlates with transcriptional and surface changes.

a. UMAP of the single cell RNA and ADT sequencing data showing the progressive pseudotime of the gut CD8$^+$ T cell response. Color-coding indicates the pseudotime, as indicated in the legend. Cluster 6 was set as the starting point of the analysis. The labeling in quotation marks refers to the data in *Figure 1e*.
b. Plots representing the expression of the selected indicated genes as a function of pseudotime, as identified in *Extended Data Figure 2a*. On the x axis, the interquartile range of every cluster is indicated, to facilitate the correlation between gene expression and progression of cells through pseudotime. Color-coding is indicated in the legend.

Extended Data Figure 3. Drop in mitochondrial content underlies the transition of T cells from the lymph nodes into the intestinal tissue.

a. Representative flow cytometry plots to show the gating strategy of the human experiments represented in the paper. Cell populations analyzed were: T_N, T_{EM}, T_{CM} and T_{EMRA} from the blood; and T_{RM} from intestinal biopsies.
b. Representative flow cytometry plots to show the gating strategy of the mouse experiments represented in the paper. Cell populations analyzed were T_N, T_{EM}, T_{CM} and T_{RM} from the mLN, CD69$^-$CD103$^-$ and CD69$^+$CD103$^+$ cells from LP and T_{RM} from IEL.
c. Flow cytometry analysis of Mitotracker green staining in the indicated cell populations across the transition CD69$^-$CD103$^-$ - CD69$^+$CD103$^-$ - CD69$^+$CD103$^+$ cells isolated from LP of unchallenged C57BL/6J mice. Color-coding is as per legend. The flow cytometry plot shows the gating strategy

based on CD69 and CD103 expression. Lines in the dot plot show mean values and the data are representative of n = 9 independent experiments. Statistics were performed using one-way ANOVA and Tukey's multiple comparison correction.

d. Flow cytometry analysis of Mitotracker green staining in the indicated cell populations isolated from mLN and intestine of unchallenged C57BL/6J mice, upon treatment of cells with Verapamil. Color-coding is as per legend. Lines in the dot plot show mean values and the data are representative of n = 2 independent experiments. Statistics were performed using one-way ANOVA and Tukey's multiple comparison correction.

e. Flow cytometry analysis of Mitotracker green staining in the indicated cell populations isolated from mLN and intestine of unchallenged C57BL/6J mice, upon performing cell isolation in presence of KN-62. Lines in the dot plot show mean values and the data are representative of n = 1 experiment. Statistics were performed using one-way ANOVA and Tukey's multiple comparison correction.

f. Western blotting analysis of Tom20 and TFAM in the indicated cell populations. Dot plots show the quantification by densitometry of the levels of Tom20 and TFAM as compared to β-actin, shown in *Figure 3c*. Lines in the dot plot show mean values and the data are cumulative of n = 2-5 independent experiments.

Extended Data Figure 4. Residency in the gut impacts the structure and function of mitochondria.

a. Flow cytometry analysis of Mitotracker green staining in antigen-specific ($CD45.2^+$) OT-I cells isolated from mLN and intestine of C57BL/6J mice orally challenged with *LmOVA* and analyzed 24 days post-infection. Lines in the dot plot show mean values and data represent n = 2 independent experiments. Statistics were performed using one-way ANOVA and Tukey's multiple comparison correction.

b. Fluorescence microscopy of the indicated cell populations isolated from unchallenged PhAM mice. T_N cells were isolated from the spleen. Red lines in the dot plots indicate mean values and the plots show cumulative data of n = 2 independent experiments.

c. Western blotting analysis of OPA-1 in the indicated cell populations. β-actin loading control is the same as the one used in *Figure 3c*. The data shown are representative of n = 6 independent experiments.

d. Transmission electron microscopy of the indicated cell populations isolated from unchallenged C57BL/6J mice. Red arrowheads indicate mitochondria with dilated cristae. The panel show representative images of n = 1 experiment.

e. Principal Component Analysis (PCA) of bulk RNA sequencing data obtained from the indicated cell populations. Color-coding is as per legend. Data show n = 3 independent experiments.

f. Volcano plots showing the distribution according to fold change (FC) and *p*-value of differentially-expressed genes between the indicated cell populations, as obtained upon bulk RNA sequencing. The cellular transitions mentioned in the main text are indicated at the top of every plot. Dashed lines indicate the fold change filter of FC > 2 and FC < -2. Data show n = 3 independent experiments.

g. Heatmaps showing the expression of selected genes (Complex I of ETC and mitochondria DNA-encoded genes) of bulk RNA sequencing data obtained from the indicated cell populations. Color-coding is as per legend (white, low expression; blue, high expression) and is showing relative values within each gene. Data show n = 3 independent experiments.

Extended Data Figure 5. The sensing of PGE$_2$ via the EP4 receptor shapes the mitochondrial profile of gut-resident CD8$^+$ T cells.

a. Flow cytometry analysis of Mitotracker green staining in macrophages isolated from the indicated tissues of unchallenged C57BL/6J mice. Lines in the dot plot show mean values and the data are representative of n = 2 independent experiments.

b. Schematic representation of the *in vitro* cell culture to generate (IL-2)-T cells and (IL-15/TGF-β)-T cells. Further details can be found in the Methods section.

c. Flow cytometry analysis of the surface expression of the indicated markers in (IL-2)-T cells and (IL-15/TGF-β)-T cells 6 days after activation. Lines in the dot plots show mean values and the data are representative of n = 3 independent experiments.

d, e. Flow cytometry analysis of Mitotracker green (*d*) and TMRM (*e*) staining in CD8$^+$ T cells activated in IL-2- or IL-15/TGF-β-polarizing conditions for 6 days and treated for 24 hours with 100 nM PGE$_2$. Lines in the dot plot show mean values and the data are representative of n = 2 independent experiments. Statistics were performed using two-tailed Student's *t* test.

f. Flow cytometry analysis of Mitotracker green and TMRM staining in CD8$^+$ T cells activated in (IL-15/TGF-β)-T cell-polarizing conditions for 5 days and treated for 24 hours with different concentrations of PGE$_2$. Lines in the dot plot show mean values and the data are representative of n = 2 independent experiments. Statistics were performed using one-way ANOVA and Dunnet's multiple comparison correction.

g. Heatmaps show the expression of selected genes of bulk RNA sequencing data obtained from the indicated cell populations. Color-coding is as per legend (white, low expression; blue, high expression) and shows relative values within each gene. Data show n = 3 independent experiments.

h. Western blotting analysis of EP4 in CD8$^+$ T cells isolated from C57BL/6J mice, treated for CRISPR-Cas9-mediated deletion of *Ptger4* and activated in (IL-15/TGF-β)-T cell-polarizing conditions for 6 days. The data are representative of n = 2 independent experiments. Dot plots show the quantification by densitometry of the levels of EP4 as compared to β-actin. Lines in the dot plot show mean values and the data are cumulative of n = 2 independent experiments.

i. Flow cytometry analysis of Mitotracker green and TMRM staining in CD8$^+$ T cells isolated from C57BL/6J mice, treated for CRISPR-Cas9-mediated deletion of *Ptger4* and activated in T$_{RM}$ polarizing conditions for 5 days followed by 24h treatment with 100 nM PGE$_2$. The bar graphs show the GeoMFI of Mitotracker green and the fraction of TMRM high cells. Data are representative of n

= 2 independent experiments. Statistics were performed using one-way ANOVA and Tukey's multiple comparison correction.

j. Flow cytometry analysis of the distribution of Ctrl vs *Ptger4*-deleted CD8$^+$ T cells within the population of CD45.2$^+$ cells upon *LmOVA* challenge in mLN. Lines in the dot plot show pairing within single mice, and the dot plots show cumulative data of n = 2 independent experiments. Statistics were performed using two-tailed paired *t* test.

k. Flow cytometry analysis of interferon-γ and TNF production by Ctrl vs *Ptger4*-deleted CD8$^+$ T cells within the population of CD45.2$^+$ cells isolated from LP and IEL, 7 days after *LmOVA* challenge, upon PMA+ionomycin restimulation for 4h. Lines in the dot plot show mean values; dot plots show cumulative data of n = 3 independent experiments. Statistics were performed using two-way ANOVA and Sidak's multiple comparison correction.

Extended Data Figure 6. Autophagy and glutathione are key to maintain fitness of gut-resident CD8$^+$ T cells.

a. Western blot analysis of LC3-I (non-lipidated) and LC3-II (lipidated) in the indicated cell populations, isolated in presence or absence of the autophagy inhibitor Bafilomycin A1. The dot plot shows the quantification by densitometry, in LP- and IEL-isolated cells. Lines in dot plots show mean values. Dot plots show cumulative data of n = 2 independent experiments.

b. Western blot analysis of p62 in the indicated cell populations. The bar graph shows the quantification by densitometry of the levels of p62 as compared to β-actin, shown in *Figure 5b*. Data are from n = 1 experiment.

c. Flow cytometry analysis of Mitotracker green and TMRM staining in CD8$^+$ T cells isolated from C57BL/6J mice, activated in (IL-15/TGF-β)-T cell-polarizing conditions for 5 days and treated with PGE_2 in presence of the autophagy inhibitor wortmannin. The bar graphs show the GeoMFI of Mitotracker green and the fraction of TMRM high cells. Lines in the dot plot show mean values ± SEM and the data are representative of n = 3 independent experiments. Statistics were performed using one-way ANOVA and Tukey's multiple comparison correction.

d. Flow cytometry analysis of Mitotracker green and TMRM staining in CD8$^+$ T cells isolated from C57BL/6 mice, activated in (IL-15/TGF-β)-T cell-polarizing conditions for 5 days and treated with PGE_2 in presence of the autophagy inhibitor SBI-0206965 (ULK1-inhibitor). The bar graphs show the GeoMFI of Mitotracker green and the fraction of TMRM high cells. Lines in the dot plot show mean values ± SEM and the data are representative of n = 2 independent experiments. Statistics were performed using one-way ANOVA and Tukey's multiple comparison correction.

e. Western blot analysis of Atg5 in CD8$^+$ T cells isolated from C57BL/6J mice, treated for CRISPR-Cas9-mediated deletion of *Atg5* and activated in (IL-15/TGF-β)-T cell-polarizing conditions for 6 days. The data shown are representative of n = 4 independent experiments. Dot plots show the quantification by densitometry of the levels of Atg5 as compared to β-actin. Lines in the dot plot show mean values and the data are cumulative of n = 4 independent experiments.

f. Flow cytometry analysis of the distribution of Ctrl vs *Atg5*-deleted CD8$^+$ T cells within the population of CD45.2$^+$ cells upon *LmOVA* challenge in mLN. Lines in the dot plot show pairing within single mice, and the dot plots show cumulative data of n = 3 independent experiments. Statistics were performed using two-tailed paired *t* test.

g. Representative flow cytometry plots to show the gating strategy used to quantify the fraction of cells with oxidized mitochondria, in Mito-roGFP2-Orp1 mice, as shown in Figure 5h. Diamide (oxidant) and DTT (reductant) were used to validate the gating strategy.

h. Biochemical quantification of the concentrations of GSH and GSSG, and their ratio, in the indicated cell populations. The bar graphs show concentrations of GSH and GSSG as arbitrary units (AU) per well containing 10^5 sorted cells. The bars show mean ± SEM. Data show n = 2-3 independent experiments. Statistics were performed using one-way ANOVA and Tukey's multiple comparison correction.

i. Western blot analysis of Gclc in CD8$^+$ T cells isolated from C57BL/6J mice, treated for CRISPR-Cas9-mediated deletion of *Gclc* and activated in (IL-15/TGF-β)-T cell-polarizing conditions for 6 days. The data shown are representative of n = 2 independent experiments.

Extended Data Figure 7. Reduced NAD$^+$ impinges on the glycolysis pathway

a. Mass spectrometry quantification of Hexose phosphate, fructose 1,6-bisphosphate, DHAP and PEP in the indicated cell populations. The bars show mean ± SEM. Data show n = 3 independent experiments analyzed simultaneously. Statistics were performed using one-way ANOVA and Tukey's multiple comparison correction.

b. Western blot analysis of Got-1 in CD8$^+$ T cells isolated from C57BL/6J mice, treated for CRISPR-Cas9-mediated deletion of *Got1* and activated in (IL-15/TGF-β)-T cell-polarizing conditions for 6 days. The data shown are representative of n = 2 independent experiments.

c. Flow cytometry analysis of the distribution of Ctrl vs *Got1*-deleted CD8$^+$ T cells within the population of CD45.2$^+$ cells upon *LmOVA* challenge in LP and IEL fraction. Lines in the dot plot show pairing within single mice, and the dot plots show cumulative data of n = 2 independent experiments. Statistics were performed using two-way ANOVA and Sidak's multiple comparison correction.

References

1. Lavelle, E.C. and R.W. Ward, *Mucosal vaccines - fortifying the frontiers.* Nat Rev Immunol, 2021.
2. Masopust, D., et al., *Dynamic T cell migration program provides resident memory within intestinal epithelium.* J Exp Med, 2010. **207**(3): p. 553-64.
3. Zhang, N. and M.J. Bevan, *CD8(+) T cells: foot soldiers of the immune system.* Immunity, 2011. **35**(2): p. 161-8.
4. Buck, M.D., et al., *Mitochondrial Dynamics Controls T Cell Fate through Metabolic Programming.* Cell, 2016. **166**(1): p. 63-76.
5. Doedens, A.L., et al., *Hypoxia-inducible factors enhance the effector responses of CD8(+) T cells to persistent antigen.* Nat Immunol, 2013. **14**(11): p. 1173-82.
6. Kaech, S.M., et al., *Molecular and functional profiling of memory CD8 T cell differentiation.* Cell, 2002. **111**(6): p. 837-51.
7. Pearce, E.L., et al., *Enhancing CD8 T-cell memory by modulating fatty acid metabolism.* Nature, 2009. **460**(7251): p. 103-7.
8. Mueller, S.N., et al., *Memory T cell subsets, migration patterns, and tissue residence.* Annu Rev Immunol, 2013. **31**: p. 137-61.
9. Kok, L., et al., *A committed tissue-resident memory T cell precursor within the circulating CD8+ effector T cell pool.* J Exp Med, 2020. **217**(10).
10. Milner, J.J., et al., *Heterogenous Populations of Tissue-Resident CD8(+) T Cells Are Generated in Response to Infection and Malignancy.* Immunity, 2020. **52**(5): p. 808-824 e7.
11. Bartolome-Casado, R., et al., *Resident memory CD8 T cells persist for years in human small intestine.* J Exp Med, 2019. **216**(10): p. 2412-2426.
12. Schenkel, J.M. and D. Masopust, *Tissue-resident memory T cells.* Immunity, 2014. **41**(6): p. 886-97.
13. Szabo, P.A., M. Miron, and D.L. Farber, *Location, location, location: Tissue resident memory T cells in mice and humans.* Sci Immunol, 2019. **4**(34).
14. Wijeyesinghe, S., et al., *Expansible residence decentralizes immune homeostasis.* Nature, 2021. **592**(7854): p. 457-462.
15. Christo, S.N., et al., *Discrete tissue microenvironments instruct diversity in resident memory T cell function and plasticity.* Nat Immunol, 2021. **22**(9): p. 1140-1151.
16. Mackay, L.K., et al., *Hobit and Blimp1 instruct a universal transcriptional program of tissue residency in lymphocytes.* Science, 2016. **352**(6284): p. 459-63.
17. Mackay, L.K., et al., *The developmental pathway for CD103(+)CD8+ tissue-resident memory T cells of skin.* Nat Immunol, 2013. **14**(12): p. 1294-301.
18. Mackay, L.K., et al., *T-box Transcription Factors Combine with the Cytokines TGF-beta and IL-15 to Control Tissue-Resident Memory T Cell Fate.* Immunity, 2015. **43**(6): p. 1101-11.
19. Milner, J.J., et al., *Runx3 programs CD8(+) T cell residency in non-lymphoid tissues and tumours.* Nature, 2017. **552**(7684): p. 253-257.
20. Pan, Y., et al., *Survival of tissue-resident memory T cells requires exogenous lipid uptake and metabolism.* Nature, 2017. **543**(7644): p. 252-256.
21. Frizzell, H., et al., *Organ-specific isoform selection of fatty acid-binding proteins in tissue-resident lymphocytes.* Sci Immunol, 2020. **5**(46).
22. Chang, C.H., et al., *Metabolic Competition in the Tumor Microenvironment Is a Driver of Cancer Progression.* Cell, 2015. **162**(6): p. 1229-41.
23. Ho, P.C., et al., *Phosphoenolpyruvate Is a Metabolic Checkpoint of Anti-tumor T Cell Responses.* Cell, 2015. **162**(6): p. 1217-28.
24. Li, C., et al., *The Transcription Factor Bhlhe40 Programs Mitochondrial Regulation of Resident CD8(+) T Cell Fitness and Functionality.* Immunity, 2019. **51**(3): p. 491-507 e7.
25. Reinfeld, B.I., et al., *Cell-programmed nutrient partitioning in the tumour microenvironment.* Nature, 2021. **593**(7858): p. 282-288.
26. Hayward, S.L., et al., *Environmental cues regulate epigenetic reprogramming of airway-resident memory CD8(+) T cells.* Nat Immunol, 2020. **21**(3): p. 309-320.
27. Masopust, D., et al., *Cutting edge: gut microenvironment promotes differentiation of a unique memory CD8 T cell population.* J Immunol, 2006. **176**(4): p. 2079-83.

28. Anderson, K.G., et al., *Intravascular staining for discrimination of vascular and tissue leukocytes.* Nat Protoc, 2014. **9**(1): p. 209-22.
29. Skon, C.N., et al., *Transcriptional downregulation of S1pr1 is required for the establishment of resident memory CD8+ T cells.* Nat Immunol, 2013. **14**(12): p. 1285-93.
30. Mukherji, A., et al., *Homeostasis in intestinal epithelium is orchestrated by the circadian clock and microbiota cues transduced by TLRs.* Cell, 2013. **153**(4): p. 812-27.
31. Sitkovsky, M.V. and A. Ohta, *The 'danger' sensors that STOP the immune response: the A2 adenosine receptors?* Trends Immunol, 2005. **26**(6): p. 299-304.
32. Brenes, A.J., et al., *Tissue environment, not ontogeny, defines murine intestinal intraepithelial T lymphocytes.* Elife, 2021. **10**.
33. Street, K., et al., *Slingshot: cell lineage and pseudotime inference for single-cell transcriptomics.* BMC Genomics, 2018. **19**(1): p. 477.
34. de Almeida, M.J., et al., *Dye-Independent Methods Reveal Elevated Mitochondrial Mass in Hematopoietic Stem Cells.* Cell Stem Cell, 2017. **21**(6): p. 725-729 e4.
35. Scheuplein, F., et al., *NAD+ and ATP released from injured cells induce P2X7-dependent shedding of CD62L and externalization of phosphatidylserine by murine T cells.* J Immunol, 2009. **182**(5): p. 2898-908.
36. Pham, A.H., J.M. McCaffery, and D.C. Chan, *Mouse lines with photo-activatable mitochondria to study mitochondrial dynamics.* Genesis, 2012. **50**(11): p. 833-43.
37. Del Dotto, V., et al., *OPA1 Isoforms in the Hierarchical Organization of Mitochondrial Functions.* Cell Rep, 2017. **19**(12): p. 2557-2571.
38. Reinhardt, R.L., H.E. Liang, and R.M. Locksley, *Cytokine-secreting follicular T cells shape the antibody repertoire.* Nat Immunol, 2009. **10**(4): p. 385-93.
39. Miyoshi, H., et al., *Prostaglandin E2 promotes intestinal repair through an adaptive cellular response of the epithelium.* EMBO J, 2017. **36**(1): p. 5-24.
40. Patankar, J.V., et al., *E-type prostanoid receptor 4 drives resolution of intestinal inflammation by blocking epithelial necroptosis.* Nat Cell Biol, 2021. **23**(7): p. 796-807.
41. Sanin, D.E., et al., *Mitochondrial Membrane Potential Regulates Nuclear Gene Expression in Macrophages Exposed to Prostaglandin E2.* Immunity, 2018. **49**(6): p. 1021-1033 e6.
42. Palikaras, K., E. Lionaki, and N. Tavernarakis, *Mechanisms of mitophagy in cellular homeostasis, physiology and pathology.* Nat Cell Biol, 2018. **20**(9): p. 1013-1022.
43. Narendra, D., et al., *Parkin is recruited selectively to impaired mitochondria and promotes their autophagy.* J Cell Biol, 2008. **183**(5): p. 795-803.
44. Fujikawa, Y., et al., *Mouse redox histology using genetically encoded probes.* Sci Signal, 2016. **9**(419): p. rs1.
45. Gutscher, M., et al., *Proximity-based protein thiol oxidation by H2O2-scavenging peroxidases.* J Biol Chem, 2009. **284**(46): p. 31532-40.
46. Lian, G., et al., *Glutathione de novo synthesis but not recycling process coordinates with glutamine catabolism to control redox homeostasis and directs murine T cell differentiation.* Elife, 2018. **7**.
47. Mak, T.W., et al., *Glutathione Primes T Cell Metabolism for Inflammation.* Immunity, 2017. **46**(6): p. 1089-1090.
48. Smirnova, E., et al., *Dynamin-related protein Drp1 is required for mitochondrial division in mammalian cells.* Mol Biol Cell, 2001. **12**(8): p. 2245-56.
49. Burman, J.L., et al., *Mitochondrial fission facilitates the selective mitophagy of protein aggregates.* J Cell Biol, 2017. **216**(10): p. 3231-3247.
50. Song, M., et al., *Mitochondrial fission and fusion factors reciprocally orchestrate mitophagic culling in mouse hearts and cultured fibroblasts.* Cell Metab, 2015. **21**(2): p. 273-286.
51. Yamashita, S.I., et al., *Mitochondrial division occurs concurrently with autophagosome formation but independently of Drp1 during mitophagy.* J Cell Biol, 2016. **215**(5): p. 649-665.
52. Steinert, E.M., et al., *Quantifying Memory CD8 T Cells Reveals Regionalization of Immunosurveillance.* Cell, 2015. **161**(4): p. 737-49.
53. Belkaid, Y. and T.W. Hand, *Role of the microbiota in immunity and inflammation.* Cell, 2014. **157**(1): p. 121-41.
54. Jeurissen, S.H., et al., *Lymphocyte migration into the lamina propria of the gut is mediated by specialized HEV-like blood vessels.* Immunology, 1987. **62**(2): p. 273-7.

55. Beura, L.K., et al., *T Cells in Nonlymphoid Tissues Give Rise to Lymph-Node-Resident Memory T Cells.* Immunity, 2018. **48**(2): p. 327-338 e5.
56. Boniface, K., et al., *Prostaglandin E2 regulates Th17 cell differentiation and function through cyclic AMP and EP2/EP4 receptor signaling.* J Exp Med, 2009. **206**(3): p. 535-48.
57. Chinen, T., et al., *Prostaglandin E2 and SOCS1 have a role in intestinal immune tolerance.* Nat Commun, 2011. **2**: p. 190.
58. Crittenden, S., et al., *Prostaglandin E2 promotes intestinal inflammation via inhibiting microbiota-dependent regulatory T cells.* Sci Adv, 2021. **7**(7).
59. Lee, J., et al., *T cell-intrinsic prostaglandin E2-EP2/EP4 signaling is critical in pathogenic TH17 cell-driven inflammation.* J Allergy Clin Immunol, 2019. **143**(2): p. 631-643.
60. Yao, C., et al., *Prostaglandin E(2) promotes Th1 differentiation via synergistic amplification of IL-12 signalling by cAMP and PI3-kinase.* Nat Commun, 2013. **4**: p. 1685.
61. Konjar, S., et al., *Mitochondria maintain controlled activation state of epithelial-resident T lymphocytes.* Sci Immunol, 2018. **3**(24).
62. Zelenay, S., et al., *Cyclooxygenase-Dependent Tumor Growth through Evasion of Immunity.* Cell, 2015. **162**(6): p. 1257-70.
63. Morimoto, K., et al., *Cellular localization of mRNAs for prostaglandin E receptor subtypes in mouse gastrointestinal tract.* Am J Physiol, 1997. **272**(3 Pt 1): p. G681-7.
64. Mukhopadhyay, S., et al., *Loss of IL-10 signaling in macrophages limits bacterial killing driven by prostaglandin E2.* J Exp Med, 2020. **217**(2).
65. Na, Y.R., et al., *Prostaglandin E(2) receptor PTGER4-expressing macrophages promote intestinal epithelial barrier regeneration upon inflammation.* Gut, 2021. **70**(12): p. 2249-2260.
66. Kuehn, H.S., et al., *Prostaglandin E2 activates and utilizes mTORC2 as a central signaling locus for the regulation of mast cell chemotaxis and mediator release.* J Biol Chem, 2011. **286**(1): p. 391-402.
67. Swadling, L., et al., *Human Liver Memory CD8(+) T Cells Use Autophagy for Tissue Residence.* Cell Rep, 2020. **30**(3): p. 687-698 e6.
68. Ikeda, Y., et al., *Endogenous Drp1 mediates mitochondrial autophagy and protects the heart against energy stress.* Circ Res, 2015. **116**(2): p. 264-78.
69. Jiao, H., et al., *Mitocytosis, a migrasome-mediated mitochondrial quality-control process.* Cell, 2021. **184**(11): p. 2896-2910 e13.
70. Corrado, M., et al., *Macroautophagy inhibition maintains fragmented mitochondria to foster T cell receptor-dependent apoptosis.* EMBO J, 2016. **35**(16): p. 1793-809.
71. Kabat, A.M., et al., *The autophagy gene Atg16l1 differentially regulates Treg and TH2 cells to control intestinal inflammation.* Elife, 2016. **5**: p. e12444.
72. Puleston, D.J., et al., *Autophagy is a critical regulator of memory CD8(+) T cell formation.* Elife, 2014. **3**.
73. Xu, X., et al., *Autophagy is essential for effector CD8(+) T cell survival and memory formation.* Nat Immunol, 2014. **15**(12): p. 1152-61.
74. Kishton, R.J., M. Sukumar, and N.P. Restifo, *Metabolic Regulation of T Cell Longevity and Function in Tumor Immunotherapy.* Cell Metab, 2017. **26**(1): p. 94-109.
75. Gibson, G.R., E.B. Whitacre, and C.A. Ricotti, *Colitis induced by nonsteroidal anti-inflammatory drugs. Report of four cases and review of the literature.* Arch Intern Med, 1992. **152**(3): p. 625-32.
76. Konjar, S., et al., *Intestinal tissue-resident T cell activation depends on metabolite availability.* Proc Natl Acad Sci U S A, 2022. **119**(34): p. e2202144119.
77. Makaremi, S., et al., *Immune Checkpoint Inhibitors in Colorectal Cancer: Challenges and Future Prospects.* Biomedicines, 2021. **9**(9).
78. Pelly, V.S., et al., *Anti-Inflammatory Drugs Remodel the Tumor Immune Environment to Enhance Immune Checkpoint Blockade Efficacy.* Cancer Discov, 2021. **11**(10): p. 2602-2619.
79. Stuart, T., et al., *Comprehensive Integration of Single-Cell Data.* Cell, 2019. **177**(7): p. 1888-1902 e21.
80. Hafemeister, C. and R. Satija, *Normalization and variance stabilization of single-cell RNA-seq data using regularized negative binomial regression.* Genome Biol, 2019. **20**(1): p. 296.
81. Korsunsky, I., et al., *Fast, sensitive and accurate integration of single-cell data with Harmony.* Nat Methods, 2019. **16**(12): p. 1289-1296.

82. Zappia, L. and A. Oshlack, *Clustering trees: a visualization for evaluating clusterings at multiple resolutions.* Gigascience, 2018. **7**(7).
83. Young, M.D., et al., *Gene ontology analysis for RNA-seq: accounting for selection bias.* Genome Biol, 2010. **11**(2): p. R14.
84. Afgan, E., et al., *The Galaxy platform for accessible, reproducible and collaborative biomedical analyses: 2016 update.* Nucleic Acids Res, 2016. **44**(W1): p. W3-W10.
85. Ramirez, F., et al., *deepTools2: a next generation web server for deep-sequencing data analysis.* Nucleic Acids Res, 2016. **44**(W1): p. W160-5.
86. Dobin, A., et al., *STAR: ultrafast universal RNA-seq aligner.* Bioinformatics, 2013. **29**(1): p. 15-21.
87. Liao, Y., G.K. Smyth, and W. Shi, *featureCounts: an efficient general purpose program for assigning sequence reads to genomic features.* Bioinformatics, 2014. **30**(7): p. 923-30.
88. Love, M.I., W. Huber, and S. Anders, *Moderated estimation of fold change and dispersion for RNA-seq data with DESeq2.* Genome Biol, 2014. **15**(12): p. 550.
89. Wiig, H., K. Aukland, and O. Tenstad, *Isolation of interstitial fluid from rat mammary tumors by a centrifugation method.* Am J Physiol Heart Circ Physiol, 2003. **284**(1): p. H416-24.
90. Edwards-Hicks, J., et al., *Metabolic Dynamics of In Vitro CD8+ T Cell Activation.* Metabolites, 2020. **11**(1).
91. Eilertz, D., M. Mitterer, and J.M. Buescher, *automRm: An R Package for Fully Automatic LC-QQQ-MS Data Preprocessing Powered by Machine Learning.* Anal Chem, 2022. **94**(16): p. 6163-6171.

Figure 1

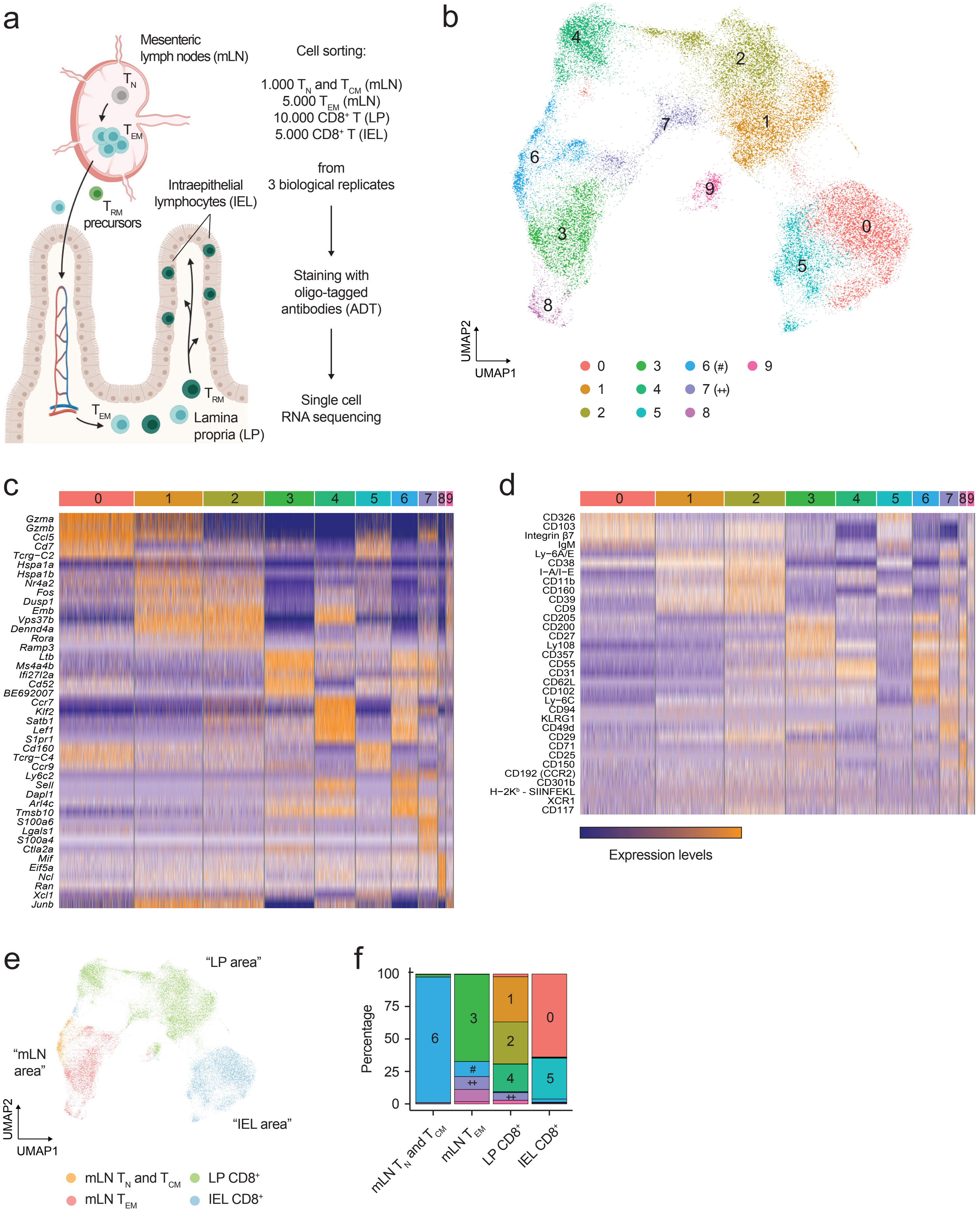
a
Mesenteric lymph nodes (mLN)
T_N
T_{EM}
T_{RM} precursors
Intraepithelial lymphocytes (IEL)
T_{RM}
T_{EM}
Lamina propria (LP)
Cell sorting:
1.000 T_N and T_{CM} (mLN)
5.000 T_{EM} (mLN)
10.000 $CD8^+$ T (LP)
5.000 $CD8^+$ T (IEL)
from
3 biological replicates
Staining with oligo-tagged antibodies (ADT)
Single cell RNA sequencing
b
0 1 2 3 4 5 6 7 8 9
UMAP2
UMAP1
0
1
2
3
4
5
6 (#)
7 (++)
8
9
c
0 1 2 3 4 5 6 7 8 9
Gzma
Gzmb
Ccl5
Cd7
Tcrg−C2
Hspa1a
Hspa1b
Nr4a2
Fos
Dusp1
Emb
Vps37b
Dennd4a
Rora
Ramp3
Ltb
Ms4a4b
Ifi27l2a
Cd52
BE692007
Ccr7
Klf2
Satb1
Lef1
S1pr1
Cd160
Tcrg−C4
Ccr9
Ly6c2
Sell
Dapl1
Arl4c
Tmsb10
S100a6
Lgals1
S100a4
Ctla2a
Mif
Eif5a
Ncl
Ran
Xcl1
Junb
d
0 1 2 3 4 5 6 7 8 9
CD326
CD103
Integrin β7
IgM
Ly−6A/E
CD38
I−A/I−E
CD11b
CD160
CD39
CD9
CD205
CD200
CD27
Ly108
CD357
CD55
CD31
CD62L
CD102
Ly−6C
CD94
KLRG1
CD49d
CD29
CD71
CD25
CD150
CD192 (CCR2)
CD301b
H−2Kᵇ - SIINFEKL
XCR1
CD117
Expression levels
e
"LP area"
"mLN area"
"IEL area"
UMAP2
UMAP1
mLN T_N and T_{CM}
mLN T_{EM}
LP $CD8^+$
IEL $CD8^+$
f
Percentage
100
75
50
25
0
6
3
#
++
1
2
4
++
0
5
mLN T_N and T_{CM}
mLN T_{EM}
LP $CD8^+$
IEL $CD8^+$

Figure 2

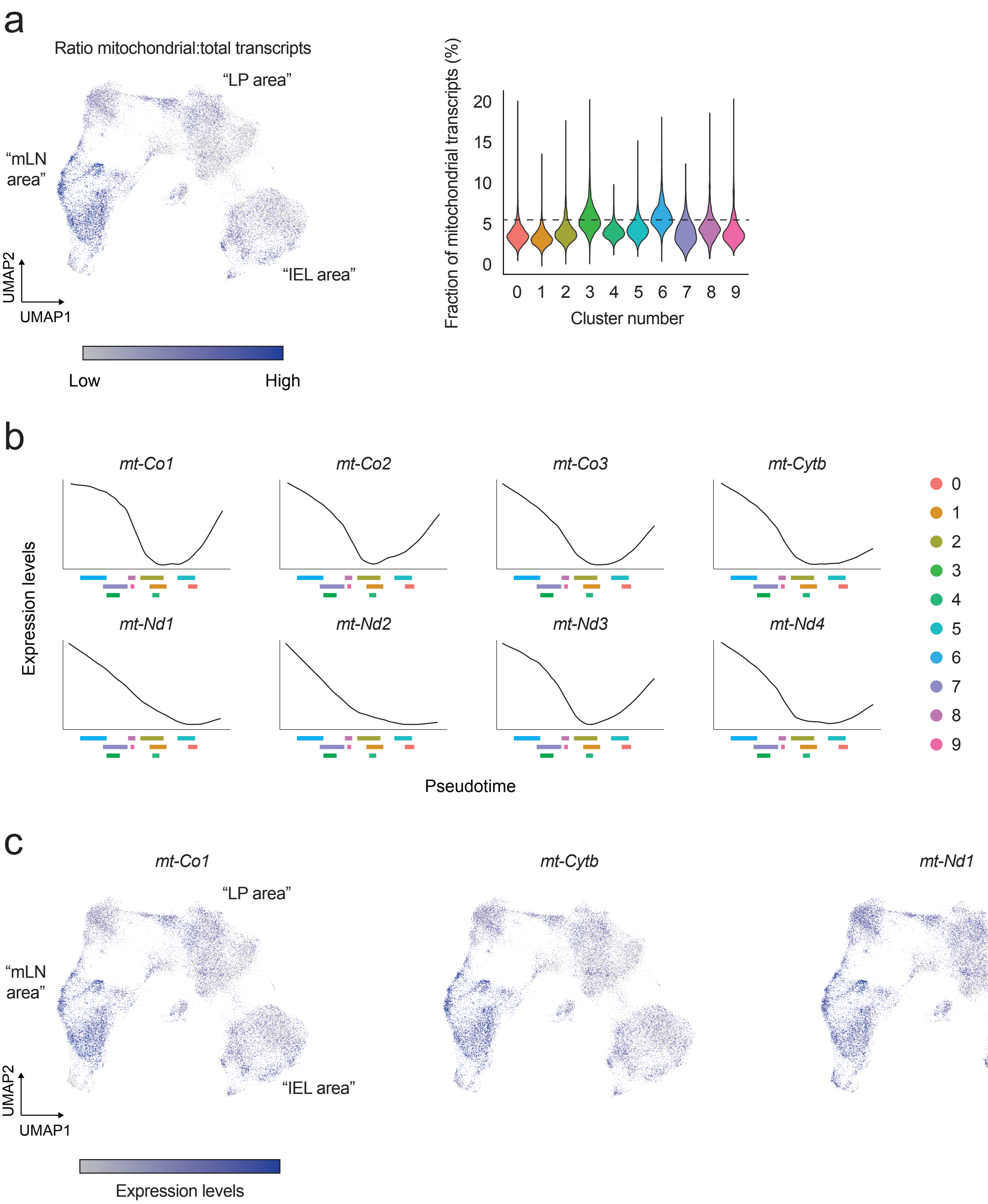
a
Ratio mitochondrial:total transcripts
"LP area"
"mLN area"
"IEL area"
UMAP2
UMAP1
Low
High
Fraction of mitochondrial transcripts (%)
20
15
10
5
0
0 1 2 3 4 5 6 7 8 9
Cluster number
b
mt-Co1
mt-Co2
mt-Co3
mt-Cytb
mt-Nd1
mt-Nd2
mt-Nd3
mt-Nd4
Expression levels
Pseudotime
0
1
2
3
4
5
6
7
8
9
c
mt-Co1
mt-Cytb
mt-Nd1
"LP area"
"mLN area"
"IEL area"
UMAP2
UMAP1
Expression levels

Figure 3

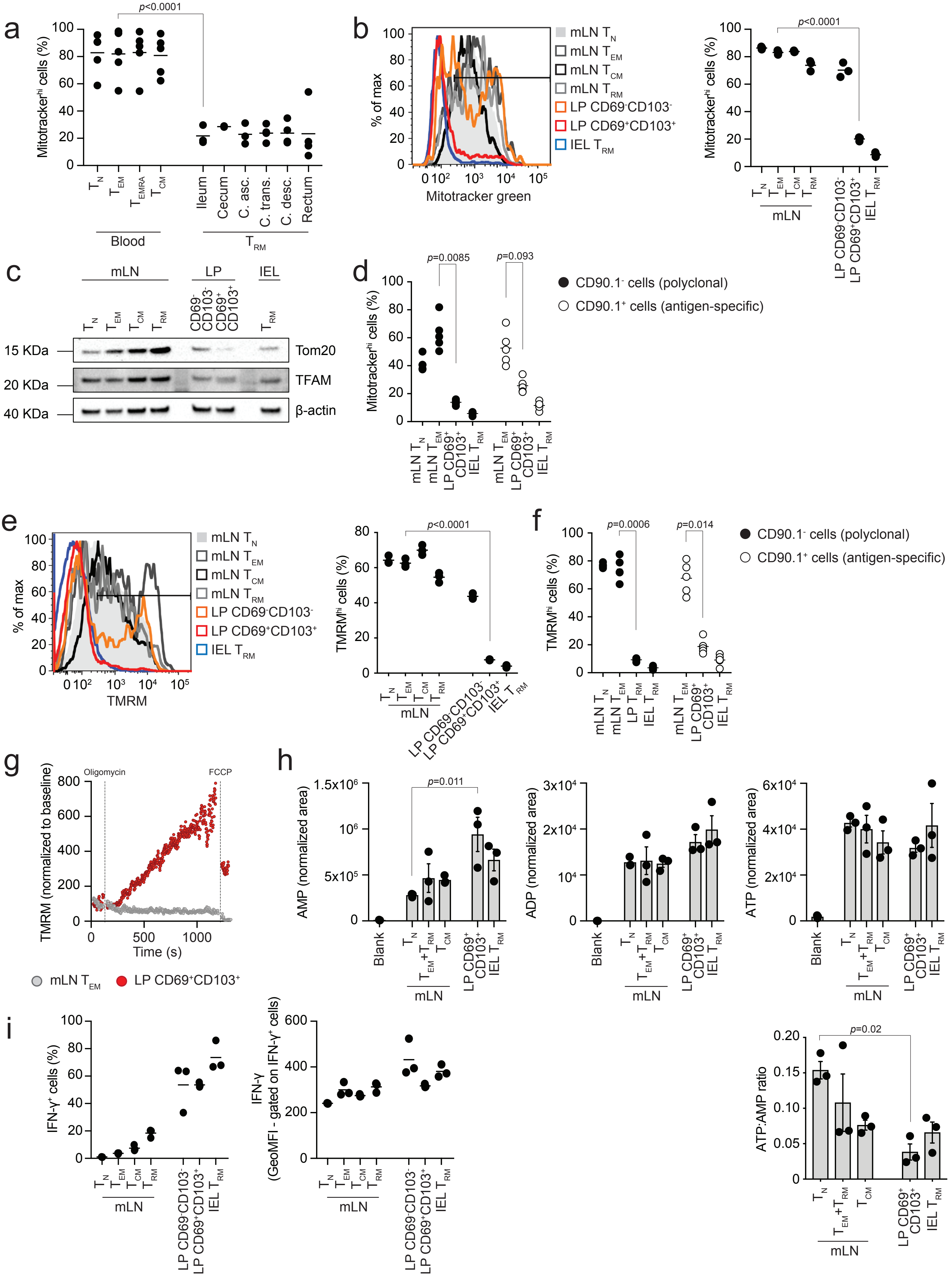
a
Mitotracker^hi cells (%)
100
80
60
40
20
0
p<0.0001
T_N
T_EM
T_EMRA
T_CM
Blood
Ileum
Cecum
C. asc.
C. trans.
C. desc.
Rectum
T_RM
b
% of max
Mitotracker green
0 10^2 10^3 10^4 10^5
mLN T_N
mLN T_EM
mLN T_CM
mLN T_RM
LP CD69^-CD103^-
LP CD69^+CD103^+
IEL T_RM
Mitotracker^hi cells (%)
p<0.0001
mLN
LP CD69^-CD103^-
LP CD69^+CD103^+
IEL T_RM
c
mLN
LP
IEL
T_N
T_EM
T_CM
T_RM
CD69^-CD103^-
CD69^+CD103^+
T_RM
15 KDa
20 KDa
40 KDa
Tom20
TFAM
β-actin
d
Mitotracker^hi cells (%)
p=0.0085
p=0.093
● CD90.1^- cells (polyclonal)
○ CD90.1^+ cells (antigen-specific)
mLN T_N
mLN T_EM
LP CD69^+CD103^+
IEL T_RM
e
% of max
TMRM
TMRM^hi cells (%)
p<0.0001
f
TMRM^hi cells (%)
p=0.0006
p=0.014
LP T_RM
g
Oligomycin
FCCP
TMRM (normalized to baseline)
800
600
400
200
0
0
500
1000
Time (s)
mLN T_EM
LP CD69^+CD103^+
h
AMP (normalized area)
1.5x10^6
10^6
5x10^5
p=0.011
ADP (normalized area)
3x10^4
2x10^4
10^4
ATP (normalized area)
6x10^4
4x10^4
2x10^4
Blank
T_N
T_EM+T_RM
T_CM
i
IFN-γ^+ cells (%)
IFN-γ (GeoMFI - gated on IFN-γ^+ cells)
600
400
200
ATP:AMP ratio
0.20
0.15
0.10
0.05
p=0.02

Figure 4

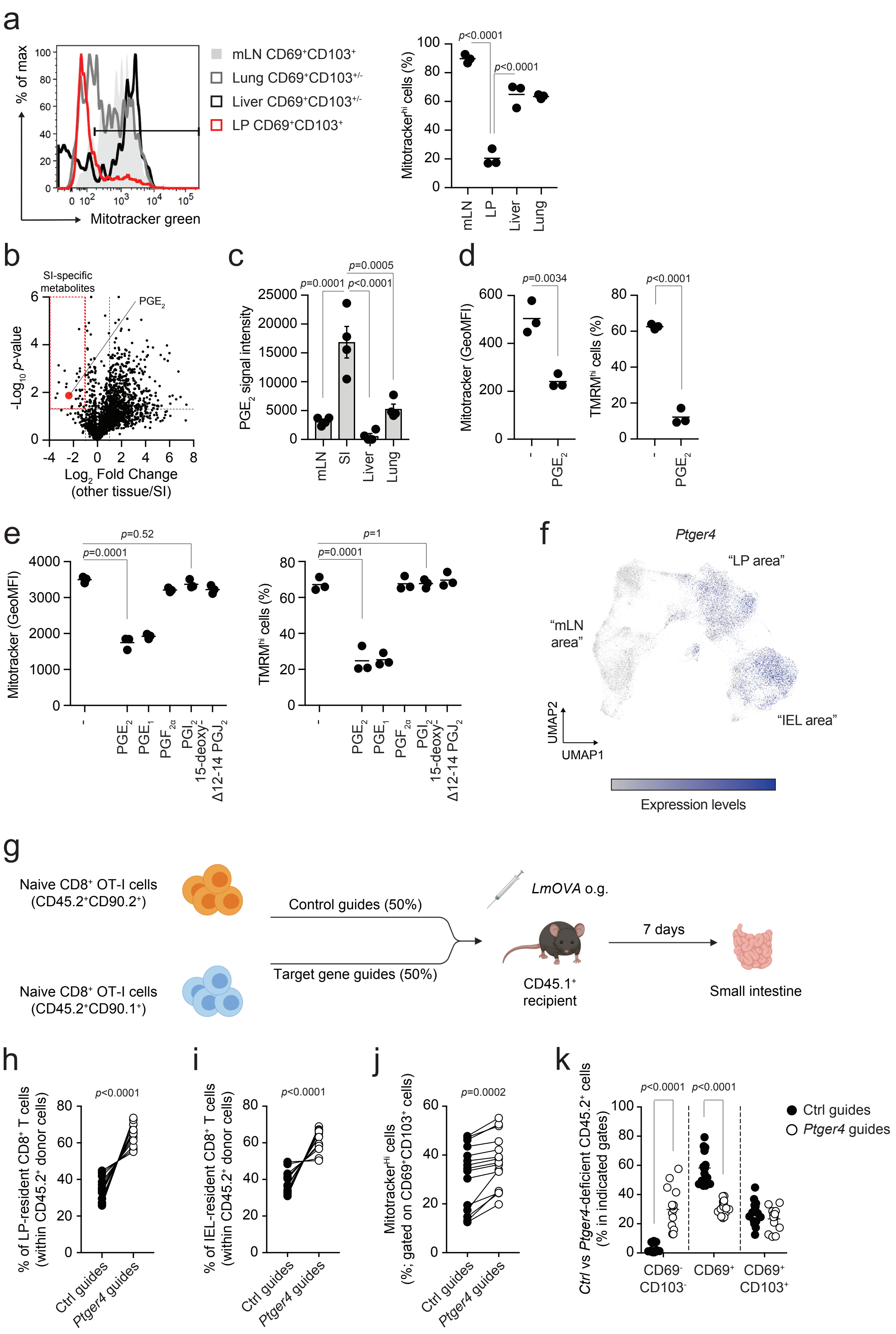
a
% of max
Mitotracker green
mLN CD69+CD103+
Lung CD69+CD103+/-
Liver CD69+CD103+/-
LP CD69+CD103+
Mitotrackerhi cells (%)
p<0.0001
p<0.0001
mLN
LP
Liver
Lung
b
SI-specific metabolites
PGE2
-Log10 p-value
Log2 Fold Change (other tissue/SI)
c
PGE2 signal intensity
p=0.0001
p<0.0001
p=0.0005
mLN
SI
Liver
Lung
d
Mitotracker (GeoMFI)
p=0.0034
TMRMhi cells (%)
p<0.0001
-
PGE2
e
Mitotracker (GeoMFI)
p=0.52
p=0.0001
TMRMhi cells (%)
p=1
p=0.0001
PGE2
PGE1
PGF2α
PGI2
15-deoxy-Δ12-14 PGJ2
f
Ptger4
"LP area"
"mLN area"
"IEL area"
UMAP2
UMAP1
Expression levels
g
Naive CD8+ OT-I cells (CD45.2+CD90.2+)
Naive CD8+ OT-I cells (CD45.2+CD90.1+)
Control guides (50%)
Target gene guides (50%)
LmOVA o.g.
CD45.1+ recipient
7 days
Small intestine
h
% of LP-resident CD8+ T cells (within CD45.2+ donor cells)
p<0.0001
Ctrl guides
Ptger4 guides
i
% of IEL-resident CD8+ T cells (within CD45.2+ donor cells)
p<0.0001
j
MitotrackerHi cells (%; gated on CD69+CD103+ cells)
p=0.0002
k
Ctrl vs Ptger4-deficient CD45.2+ cells (% in indicated gates)
p<0.0001
p<0.0001
CD69- CD103-
CD69+
CD69+ CD103+
Ctrl guides
Ptger4 guides

Figure 5

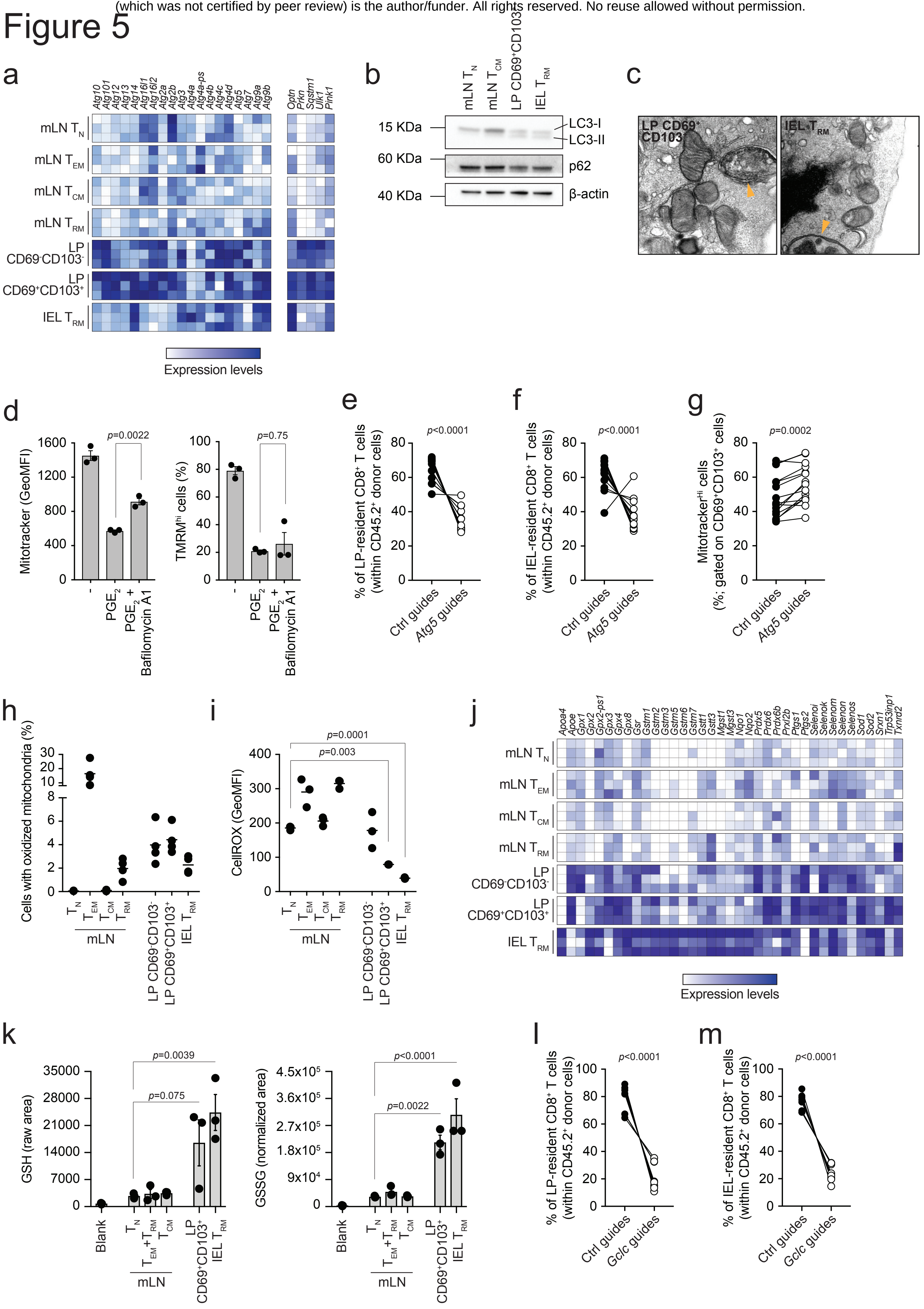
a
Atg10 Atg101 Atg12 Atg13 Atg14 Atg16l1 Atg16l2 Atg2a Atg2b Atg3 Atg4a Atg4a-ps Atg4b Atg4c Atg4d Atg5 Atg7 Atg9a Atg9b
Optn Prkn Sqstm1 Ulk1 Pink1
mLN T_N
mLN T_EM
mLN T_CM
mLN T_RM
LP CD69-CD103-
LP CD69+CD103+
IEL T_RM
Expression levels
b
mLN T_N
mLN T_CM
LP CD69+CD103+
IEL T_RM
15 KDa
60 KDa
40 KDa
LC3-I
LC3-II
p62
β-actin
c
LP CD69+ CD103+
IEL T_RM
d
Mitotracker (GeoMFI)
1600
1200
800
400
0
p=0.0022
-
PGE2
PGE2 + Bafilomycin A1
TMRMhi cells (%)
100
80
60
40
20
0
p=0.75
-
PGE2
PGE2 + Bafilomycin A1
e
% of LP-resident CD8+ T cells (within CD45.2+ donor cells)
p<0.0001
80
60
40
20
0
Ctrl guides
Atg5 guides
f
% of IEL-resident CD8+ T cells (within CD45.2+ donor cells)
p<0.0001
80
60
40
20
0
Ctrl guides
Atg5 guides
g
MitotrackerHi cells (%; gated on CD69+CD103+ cells)
p=0.0002
80
60
40
20
0
Ctrl guides
Atg5 guides
h
Cells with oxidized mitochondria (%)
30
20
10
8
6
4
2
0
T_N
T_EM
T_CM
T_RM
mLN
LP CD69-CD103-
LP CD69+CD103+
IEL T_RM
i
CellROX (GeoMFI)
p=0.0001
p=0.003
400
300
200
100
0
T_N
T_EM
T_CM
T_RM
mLN
LP CD69-CD103-
LP CD69+CD103+
IEL T_RM
j
Apoa4 Apoe Gpx1 Gpx2 Gpx2-ps1 Gpx3 Gpx4 Gpx8 Gsr Gstm1 Gstm2 Gstm3 Gstm5 Gstm6 Gstm7 Gstt1 Gstt3 Mgst1 Mgst3 Nqo1 Nqo2 Prdx5 Prdx6 Prdx6b Prxl2b Ptgs1 Ptgs2 Selenoi Selenok Selenom Selenon Selenos Sod1 Sod2 Srxn1 Trp53inp1 Txnrd2
mLN T_N
mLN T_EM
mLN T_CM
mLN T_RM
LP CD69-CD103-
LP CD69+CD103+
IEL T_RM
Expression levels
k
GSH (raw area)
p=0.0039
p=0.075
35000
28000
21000
14000
7000
0
Blank
T_N
T_EM+T_RM
T_CM
mLN
LP CD69+CD103+
IEL T_RM
GSSG (normalized area)
p<0.0001
p=0.0022
4.5x10^5
3.6x10^5
2.7x10^5
1.8x10^5
9x10^4
0
Blank
T_N
T_EM+T_RM
T_CM
mLN
LP CD69+CD103+
IEL T_RM
l
% of LP-resident CD8+ T cells (within CD45.2+ donor cells)
p<0.0001
100
80
60
40
20
0
Ctrl guides
Gclc guides
m
% of IEL-resident CD8+ T cells (within CD45.2+ donor cells)
p<0.0001
100
80
60
40
20
0
Ctrl guides
Gclc guides

Figure 6

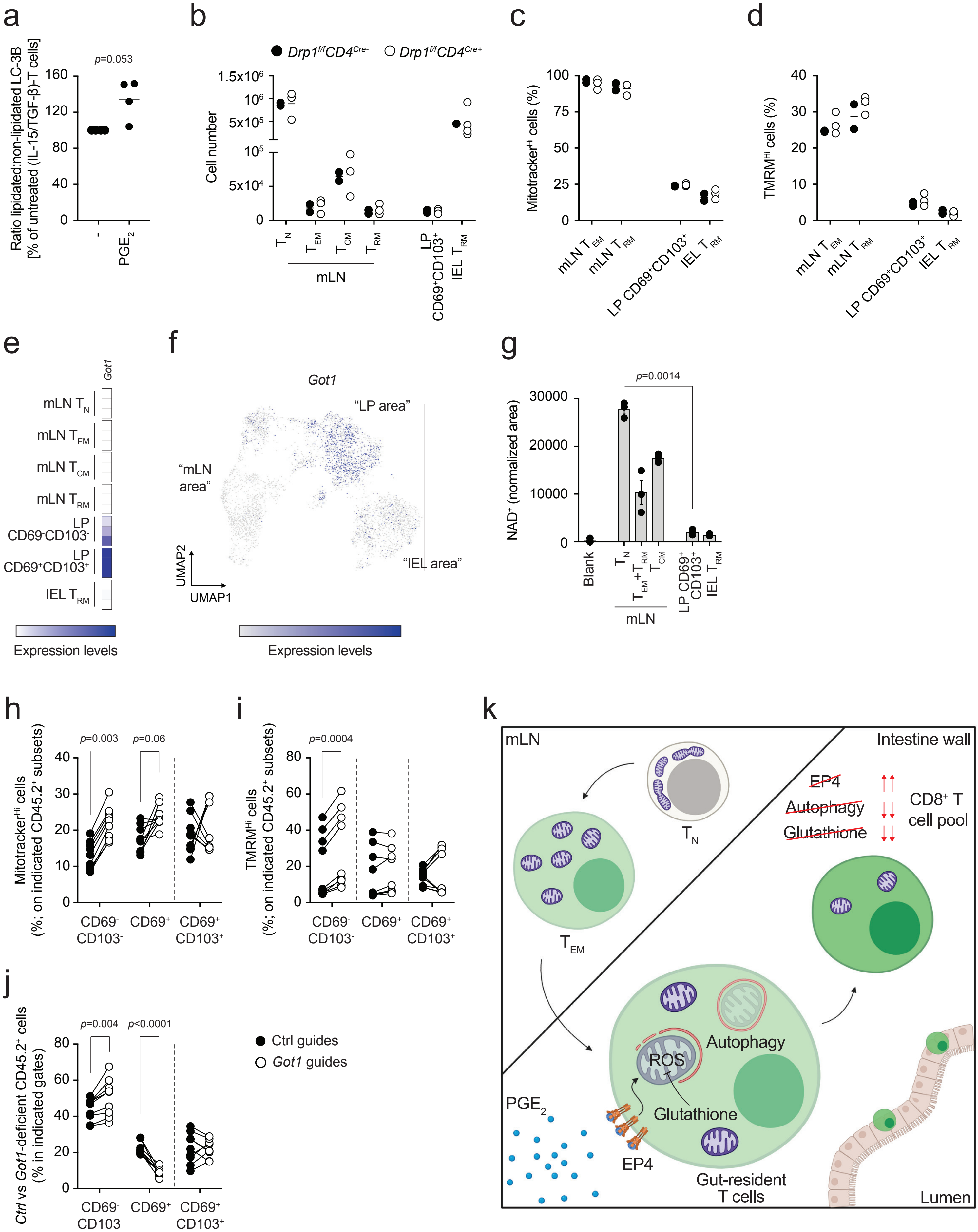
a
p=0.053
Ratio lipidated:non-lipidated LC-3B [% of untreated (IL-15/TGF-β)-T cells]
160
120
80
40
0
-
PGE2
b
● Drp1f/fCD4Cre-
○ Drp1f/fCD4Cre+
Cell number
1.5x10⁶
10⁶
5x10⁵
10⁵
5x10⁴
0
TN
TEM
TCM
TRM
mLN
LP CD69+CD103+
IEL TRM
c
Mitotracker Hi cells (%)
100
75
50
25
0
mLN TEM
mLN TRM
LP CD69+CD103+
IEL TRM
d
TMRM Hi cells (%)
40
30
20
10
0
mLN TEM
mLN TRM
LP CD69+CD103+
IEL TRM
e
Got1
mLN TN
mLN TEM
mLN TCM
mLN TRM
LP CD69-CD103-
LP CD69+CD103+
IEL TRM
Expression levels
f
Got1
"LP area"
"mLN area"
"IEL area"
UMAP2
UMAP1
Expression levels
g
p=0.0014
NAD+ (normalized area)
30000
20000
10000
0
Blank
TN
TEM+TRM
TCM
mLN
LP CD69+CD103+
IEL TRM
h
p=0.003
p=0.06
Mitotracker Hi cells (%; on indicated CD45.2+ subsets)
40
30
20
10
0
CD69- CD103-
CD69+
CD69+ CD103+
i
p=0.0004
TMRM Hi cells (%; on indicated CD45.2+ subsets)
80
60
40
20
0
CD69- CD103-
CD69+
CD69+ CD103+
j
p=0.004
p<0.0001
Ctrl vs Got1-deficient CD45.2+ cells (% in indicated gates)
80
60
40
20
0
CD69- CD103-
CD69+
CD69+ CD103+
● Ctrl guides
○ Got1 guides
k
mLN
Intestine wall
TN
TEM
EP4
Autophagy
Glutathione
CD8+ T cell pool
ROS
Autophagy
Glutathione
PGE2
EP4
Gut-resident T cells
Lumen

Extended Data Figure 1

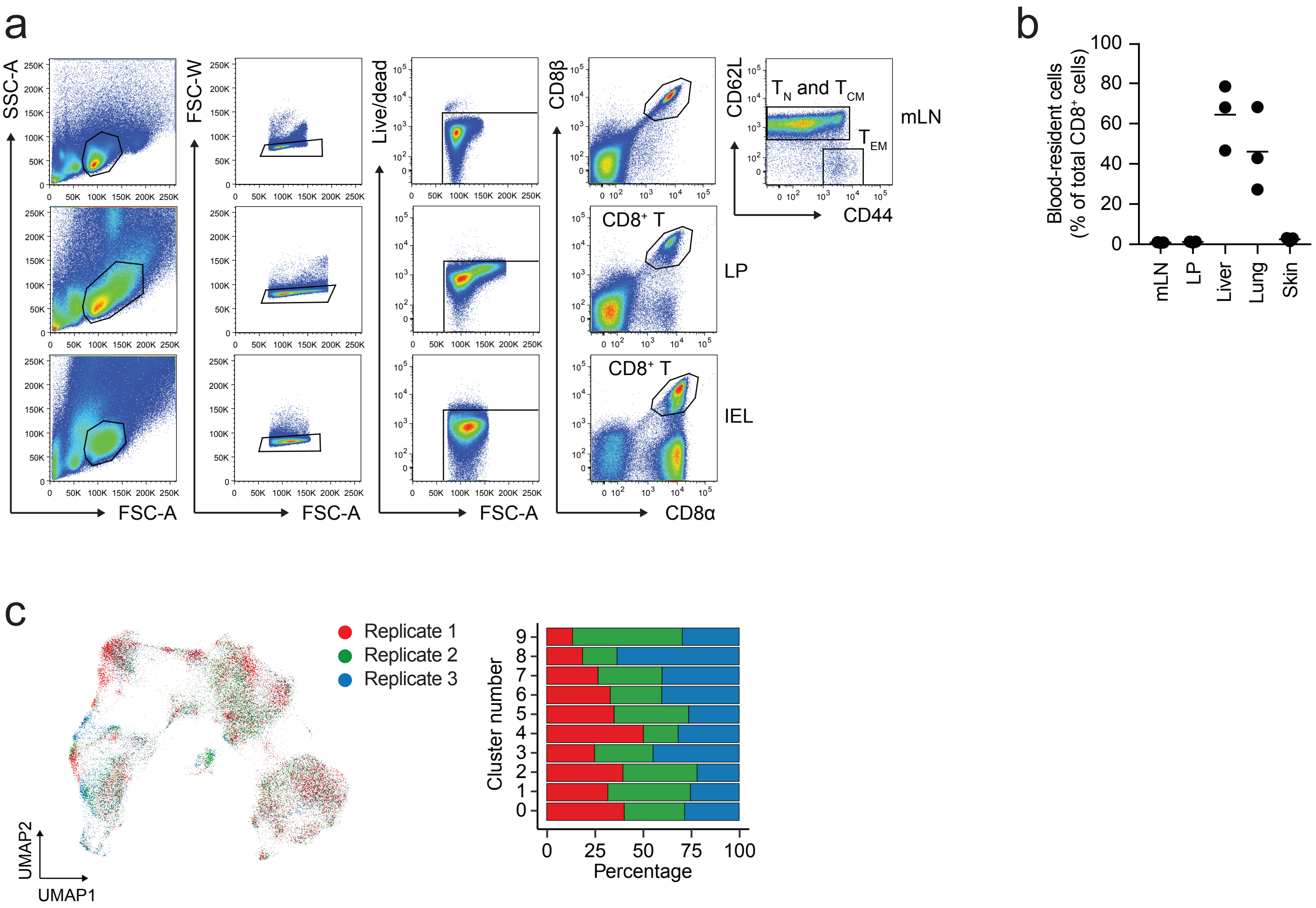

Extended Data Figure 2

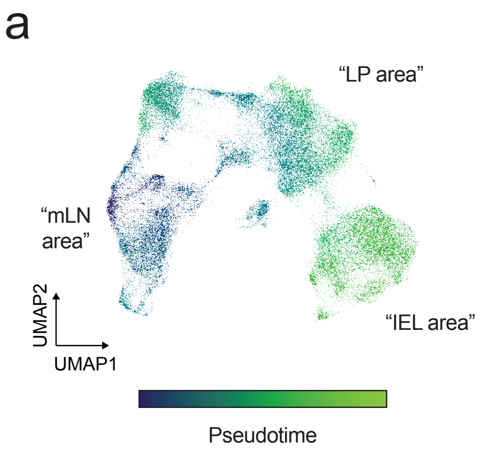

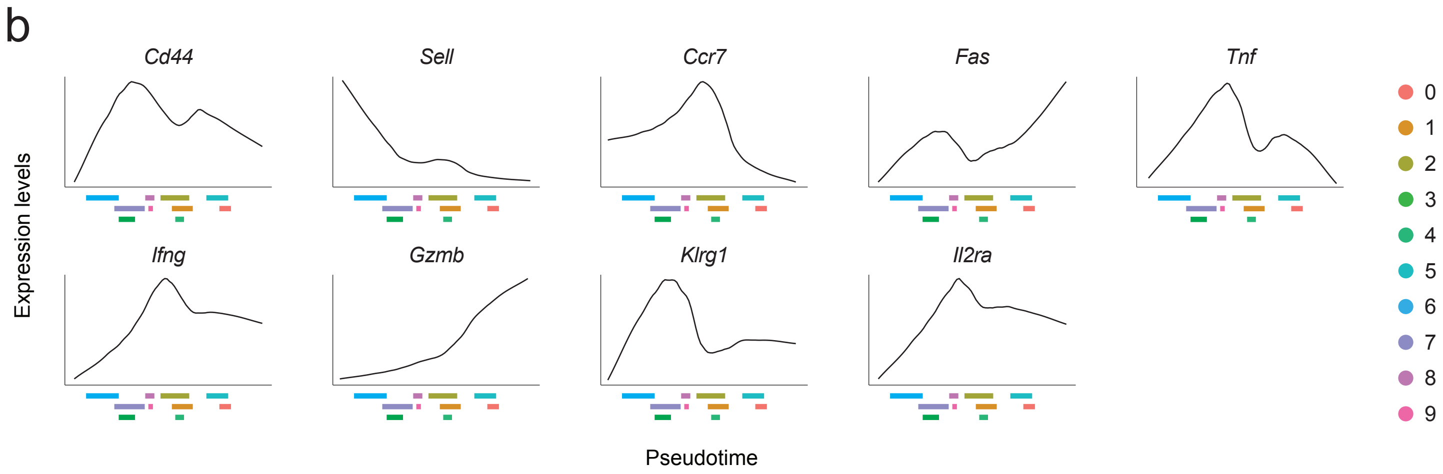

Extended Data Figure 3

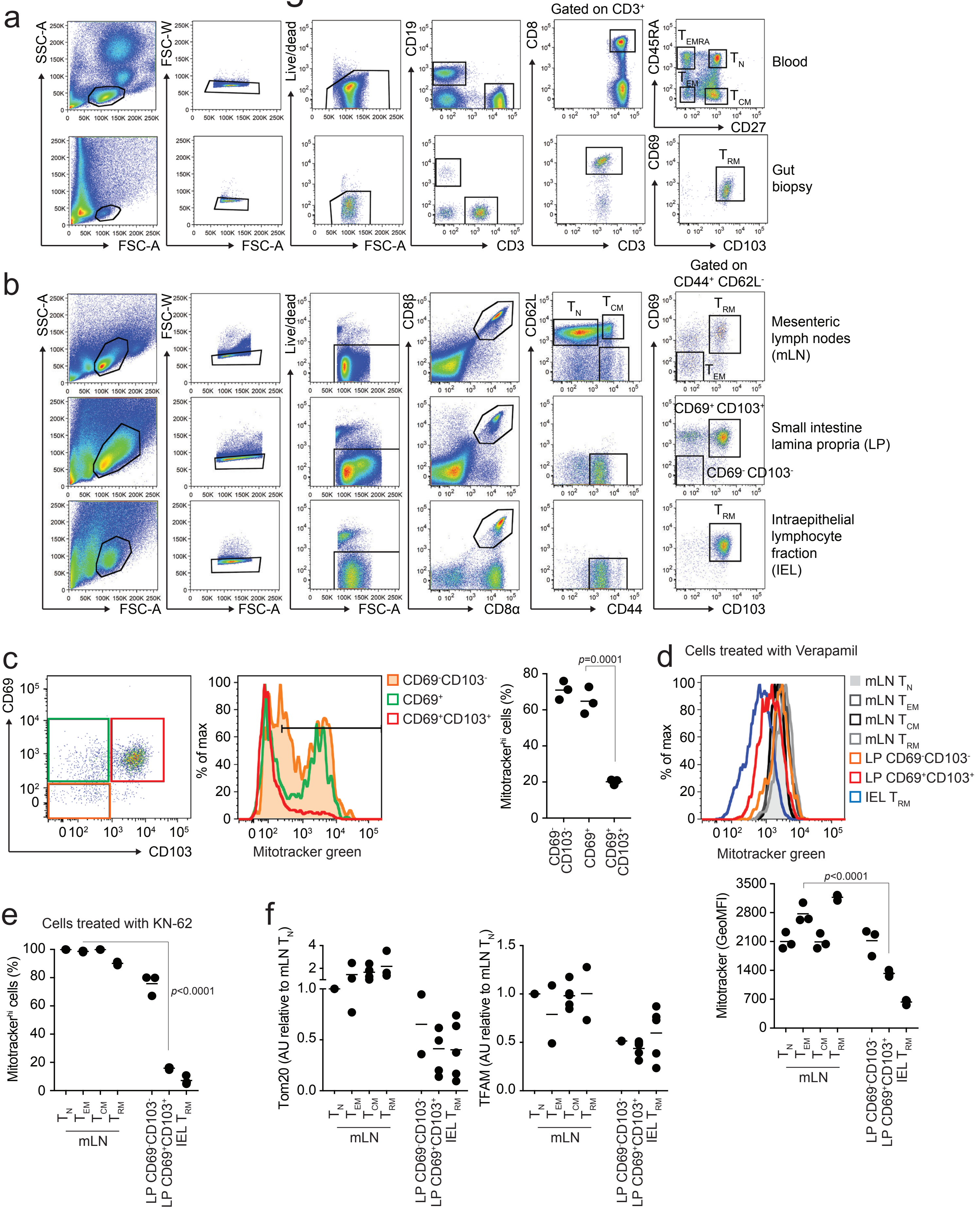

Extended Data Figure 4

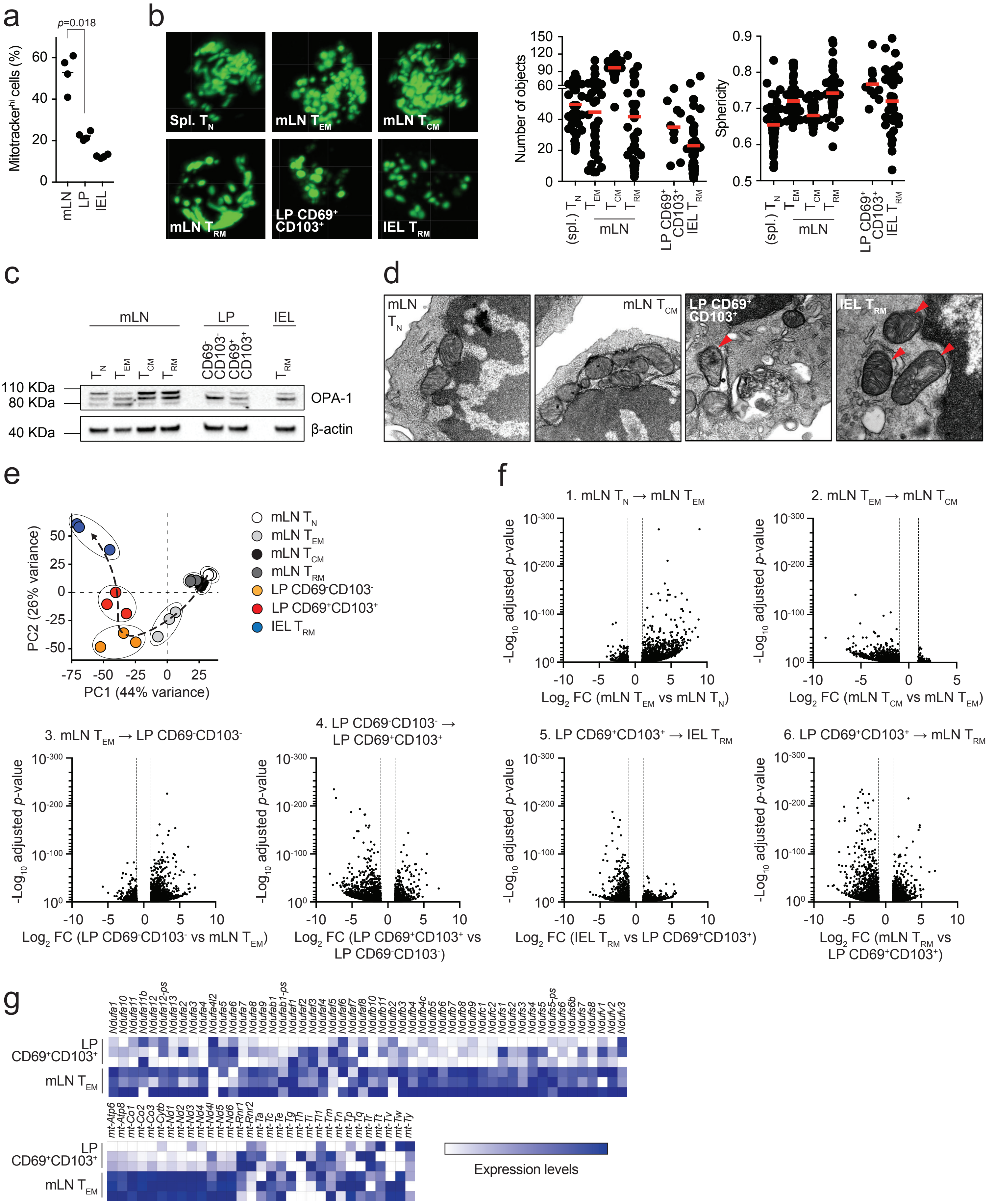

Extended Data Figure 5

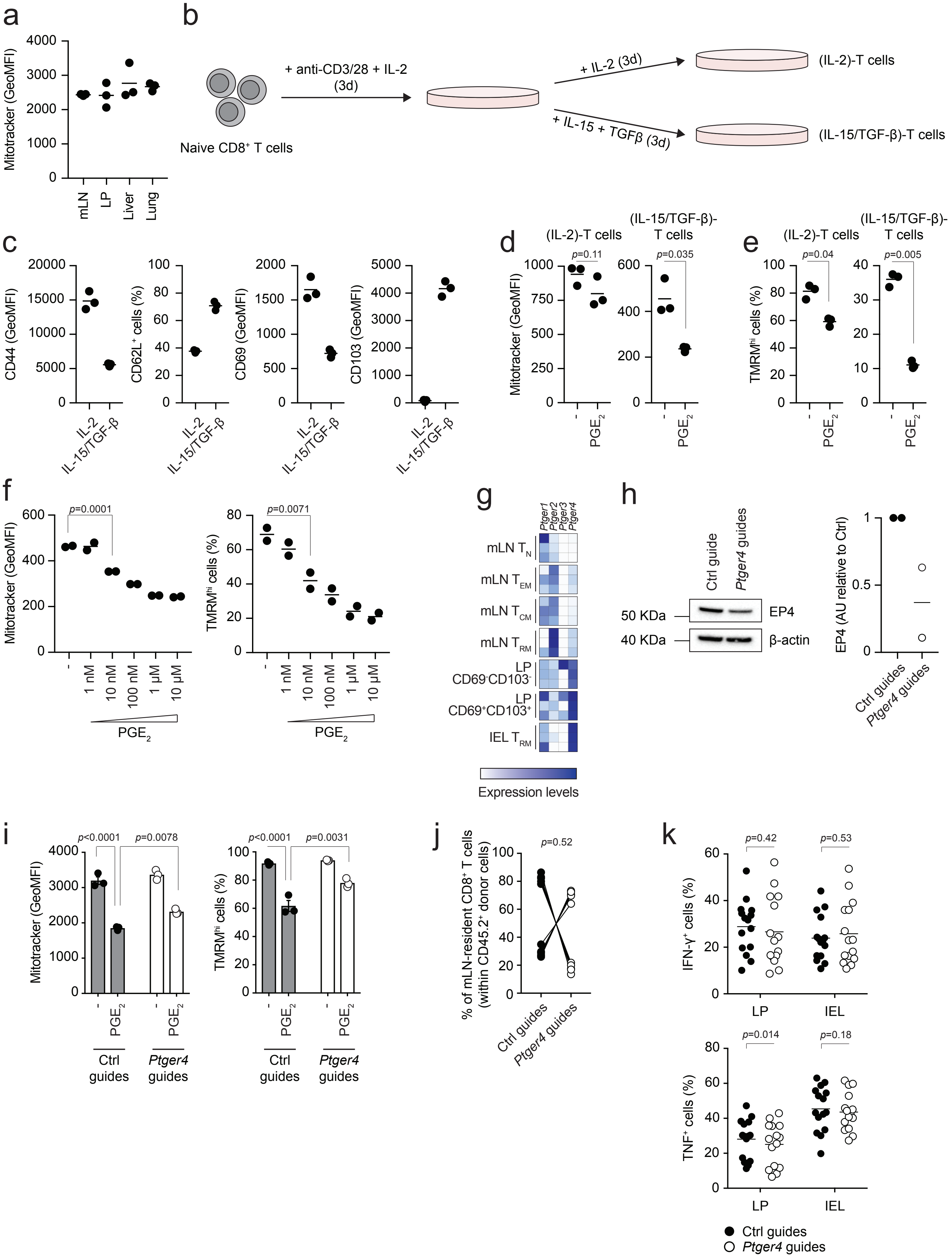

Extended Data Figure 6

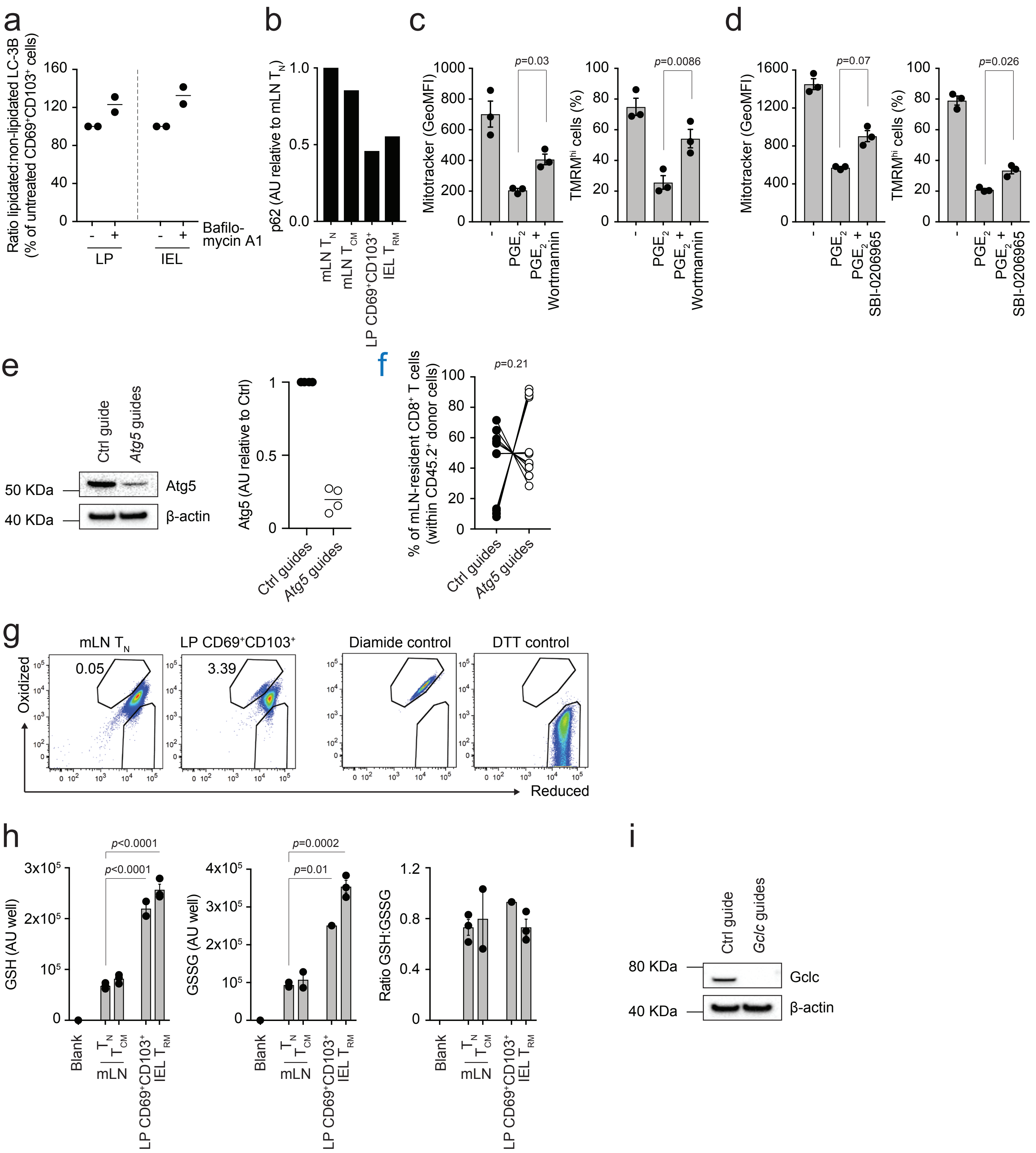

Extended Data Figure 7